Award Number:

W81XWH-09-1-0609

TITLE:
Acquisition of High Field Nuclear Magnetic Resonance Spectrometers for Research in Molecular structure, Function and Dynamics

PRINCIPAL INVESTIGATOR:

George Pack, Ph.D.

CONTRACTING ORGANIZATION:

University of Louisville
Louisville, KY 40208-1838

REPORT DATE:

September 2010

TYPE OF REPORT:
Annual

PREPARED FOR: U.S. Army Medical Research and Materiel Command
Fort Detrick, Maryland 21702-5012

DISTRIBUTION STATEMENT:

Approved for public release; distribution unlimited

REPORT DOCUMENTATION PAGE

Form Approved
OMB No. 0704-0188

1. REPORT DATE *(DD-MM-YYYY)*	2. REPORT TYPE	3. DATES COVERED *(From - To)*
September 2010	Annual	10 AUG 2009 - 9 AUG 2010

4. TITLE AND SUBTITLE

Acquisition of High Field Nuclear Magnetic Resonance Spectrometers for Research in Molecular structure, Function and Dynamics

5a. CONTRACT NUMBER

5b. GRANT NUMBER
W81XWH-09-1-0609

5c. PROGRAM ELEMENT NUMBER

6. AUTHOR(S)
George Pack, Eugene Mueller, Muriel Maurer, M. Cecilia Yappert, Richard Wittebort

George.Pack@louisville.edu

5d. PROJECT NUMBER

5e. TASK NUMBER

5f. WORK UNIT NUMBER

7. PERFORMING ORGANIZATION NAME(S) AND ADDRESS(ES)
University of Louisville

Louisville, KY 40208-1838

8. PERFORMING ORGANIZATION REPORT NUMBER

9. SPONSORING / MONITORING AGENCY NAME(S) AND ADDRESS(ES)

U.S. Army Medical Research and Materiel Command
Fort Detrick, Maryland 21702- 5012

10. SPONSOR/MONITOR'S ACRONYM(S)

11. SPONSOR/MONITOR'S REPORT NUMBER(S)

12. DISTRIBUTION / AVAILABILITY STATEMENT

Approved for public release; distribution unlimited.

13. SUPPLEMENTARY NOTES

14. ABSTRACT

Two High-Field NMR spectrometers supported four research projects:
Task 1, Mechanism of conversion of uridine to pseudouridine and to 4-thiouridine. We overexpressed the active C-terminal domain of enzyme ThiI, required for 4-thiouridine modification of tRNA. The two psuedouridine synthetases, TruB and RluA convert uridine to pseudourine in tRNA. We show the two enzymes generate the same products of F^5U.
Task 2, Devising new nanocomposites that can enhance wound healing. We synthesized MgO nanoparticles and characterized their interactions with ATP.
Task 3. Characterization of the complex between Factor XIII and fibrinogen in blood clotting. We have set up the expression system for Fbg αC 242-424 in Ecoli. A system that will subsequently be used to purify the expressed protein has been established.
Task 4. NMR probes for elastin spectroscopy built and tested. An expression system for heterodimeric collagen has been established. The entropy of water molecules on the surface of elastin has been measured.

15. SUBJECT TERMS RNA modification; nanocomposites for wound healing; factor XIII in blood clots; tensile properties of proteins.

16. SECURITY CLASSIFICATION OF:			17. LIMITATION OF ABSTRACT	18. NUMBER OF PAGES	19a. NAME OF RESPONSIBLE PERSON
a. REPORT	b. ABSTRACT	c. THIS PAGE	UU	33	USAMRMC
u	U	U			19b. TELEPHONE NUMBER *(include area code)*

Table of Contents

APPROVED SOW:

Task 1. Mechanism of conversion of uridine to pseudouridine and to 4-thiouridine (Dr. E. G. Mueller).

Year 1. Express unlabeled and carbon-13 and nitrogen-15 labeled C-terminal domain and begin acquiring and assigning spectra.

Year 2. Finish acquiring and assigning spectra; begin using distant constraints to establish the structure.

Year 3. Finish the structural determination; dock the C-terminal domain with the threaded N-terminal domain model.

Task 2. Devising new nanocomposites that can enhance wound healing (Dr. M. C. Yappert).

Year 1. Synthesize magnesia nanoparticles that effectively bind ATP and other polar compounds.

a. Sequential preparation of MgO/ATP nanocomposites.

b. Characterize the interactions between MgO nanoparticles and ATP.

Task 3. Characterization of the complex between Factor XIII and fibrinogen (Dr. M. C. Maurer).

Year 1. *E. coli* systems for expressing and purifying _C 242-424 will be optimized for producing the large amounts of isotopically labeled protein needed for NMR studies. We anticipate that both wild type and selected mutants will be desired for the studies. Unlabeled recombinant wild type FXIII A_2 and human derived FXIII B_2 will also be collected. Assessing NMR chemical shift assignments will begin.

Year 2. The structural features of the _C 242-424 segments will be determined and the sites of contact and reactivity with FXIII A_2 and B_2 will be started.

Year 3. Examine the dynamic properties of the _C 242-424 system.

d. Tensile properties of fibrous proteins (Dr. R. J. Wittebort)

Year 1: Complete 13C, 2H and 17O NMR of elastin to test hypothesis I. Publish results on elastin's mechanism of elasticity. Express and purify collagen constructs.

PROGRESS AGAINST APPROVED SOW:

Task 1 Mechanism of conversion of uridine to pseudouridine and to 4-thiouridine (Dr. E. G. Mueller).

Year 1. Express unlabeled and carbon-13 and nitrogen-15 labeled C-terminal domain and begin acquiring and assigning spectra.

The overexpression of the C-terminal domain of ThiI in minimal medium and its subsequent purification have been successfully carried out using an established protocol.[1] After 4 h induction, the bacteria were pelleted, resuspended, and lysed. The lysate was subjected to purification over a "nickel column", and the His_6•tagged C-terminal domain of ThiI was eluted with buffer containing imidazole (250 mM) and collected in two fractions. SDS-PAGE analysis (Figure **1**) revealed that even though an obvious band was observed during induction (lanes A-E), the C-terminal domain was obtained in reasonable purity and yield: 5.38 mg (400 nmol) from 500 mL culture.

Even allowing for a modest decrease in total yield during a "polishing" step of protein purification, these results establish the practicality of producing sufficient quantities of C-terminal domain in minimal medium for NMR studies. With the 700 MHz spectrometer now functional, the time is ripe to move forward with the production of labeled protein and data acquisition.

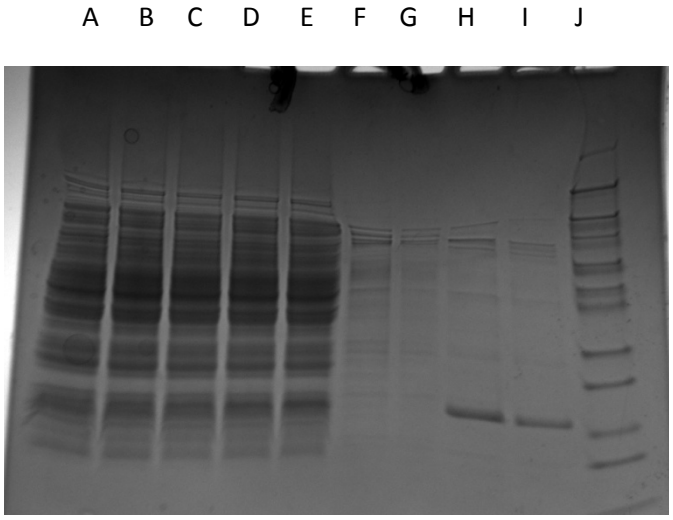

Figure 1. SDS-PAGE analysis of the induction (A-E) and purification (F-I) of the His_6•tagged C-terminal domain of ThiI. Samples of total protein prepared from aliquots of the overexpression culture were loaded onto a gradient (4-20%) gel in volumes normalized for cell density and run using tricine (rather than glycine) in the anode buffer, which effects better resolution of small proteins. A, just before induction; B-E, 1 h, 2 h, 3 h, and 4h after induction, respectively. F-G, the first and second washes of the loaded Ni-NTA (Novagen) column; H-I, the first and second elution fractions showing the expected band (13.3 kDa) for the His_6•tagged C-terminal domain. J, molecular weight markers.

[1]Marley, J., Lu, M and Bracken, C. *J. Biomol. NMR*, **2001**, *20*, 71-75.

The degradation of the 3′-nucleoside of a dinucleotide.

Two products of F^5U after the action of TruB were partially resolved by HPLC, and NMR characterization of the mixture of the products revealed that they were dinucleotides rather than the expected nucleosides because S1 nuclease does not cleave after nucleosides with nonplanar bases such as the hydrated, rearranged products of F^5U. The two products could conceivably be distinct conformers that interconvert only slowly rather than discrete stereoisomers, so it was proposed to remove the 3′ nucleoside by cleaving it with periodate and subsequent elimination of the remnants by base treatment. The method proceeded well with two model dinucleotides and then was carried out on the mixture of dinucleotide products of F^5U from the action of TruB.

The acquisition of spectral data for the [mononucleotide] product(s) of F^5U

The spectrum of the resulting mononucleotide product(s) (Figure **2**) was very similar to that of the major product of F^5U in the dinucleotide. As foreseen, the periodate cleavage/base treatment/ion exchange purification led to the loss of approximately half of the sample on a molar basis (which is roughly 75% of the NMR signal since one half of the original dinucleotide products was degraded), so the signal to noise ratio of the spectrum falls well short of ideal. Additionally, the yield also leaves it uncertain whether or not periodate cleavage itself caused the disappearance of the minor product (which would argue for the two products being constrained conformers or for the peculiar susceptibility of the minor isomer to periodate or base treatment) or whether the level of sample loss resulted in an undetectably small amount of the minor product. The sample will be re-run on the 700 MHz instrument to benefit from its greater sensitivity in looking for a small percentage of a mononucleotide product corresponding to the minor dinucleotide product, for such an observation would make it much less likely that the two dinucleotide products are constrained conformers.

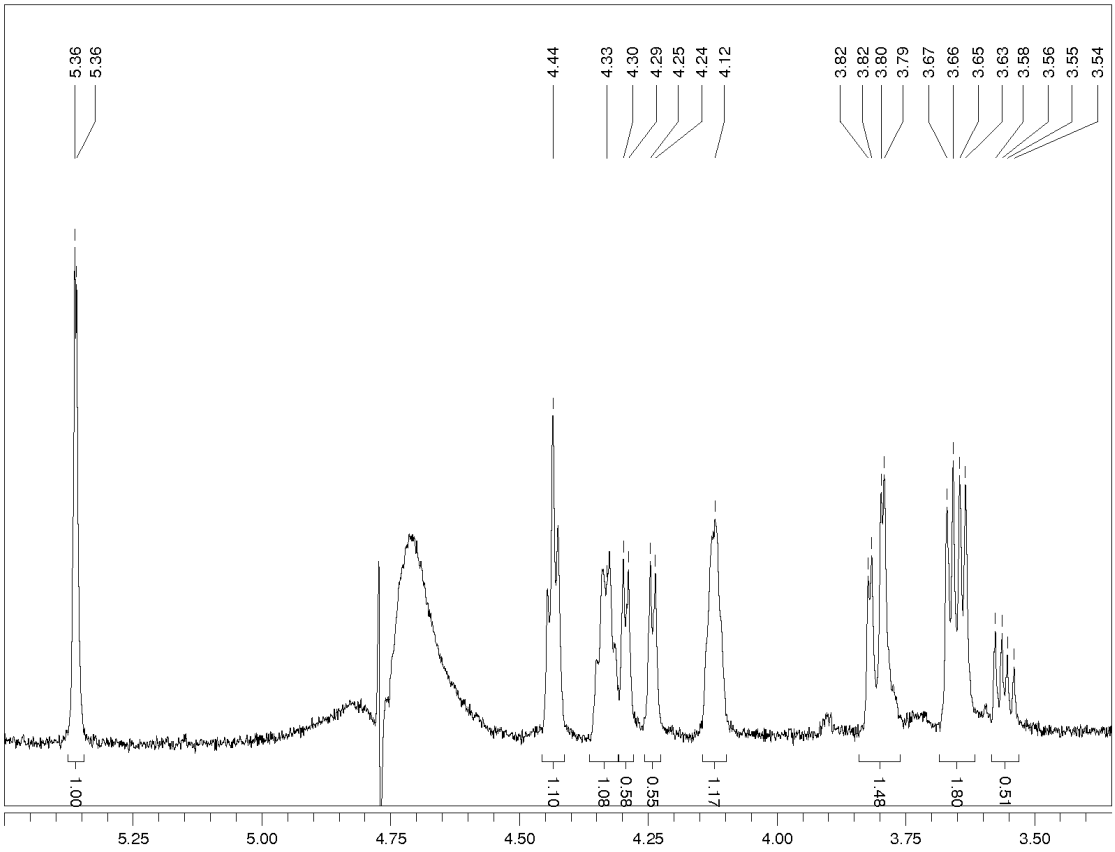

The acquisition of spectral data for the dinucleotide product(s) of F^5U from the action of RluA on stem-loop $[F^5U]$RNA.

Figure 2. The ^{1}H NMR spectrum of the mononucleotide product resulting from the periodate cleavage/base treatment/anion exchange chromatography of the dinucleotide products of F^5U from the action of TruB.

It was feared that the greater sensitivity of the 700 MHz would also be required to acquire suitable spectra of the products of F^5U from the action of RluA since this enzyme forms a stoichiometric adduct with the [F^5U]RNA so that the products would have to be purified away from a full equivalent of protein (rather than a catalytic amount of TruB, which treats [F^5U]RNA as a substrate and achieves multiple turnovers). Happily, however, the technical difficulties in obtaining sufficient quantities of the product(s) of F^5U after the action of RluA were not insurmountable, and sufficient quantities of products were obtained to acquire high quality spectra.

The 1D spectrum afforded a surprise. Even though only a single product peak is detected by C_{18} HPLC, the NMR spectrum of that peak showed that it contained two products of F^5U with very similar spectra to the major and minor products obtained by the action of TruB (Figure **3**). The most salient (yet trivial) differences arise from the identity of the 3′ nucleoside in the dinucleotide products, which is C for the "TruB products" and U for the "RluA products" (because of the sequences of the stem-loop RNAs); the HPLC column simply does not resolve the latter.

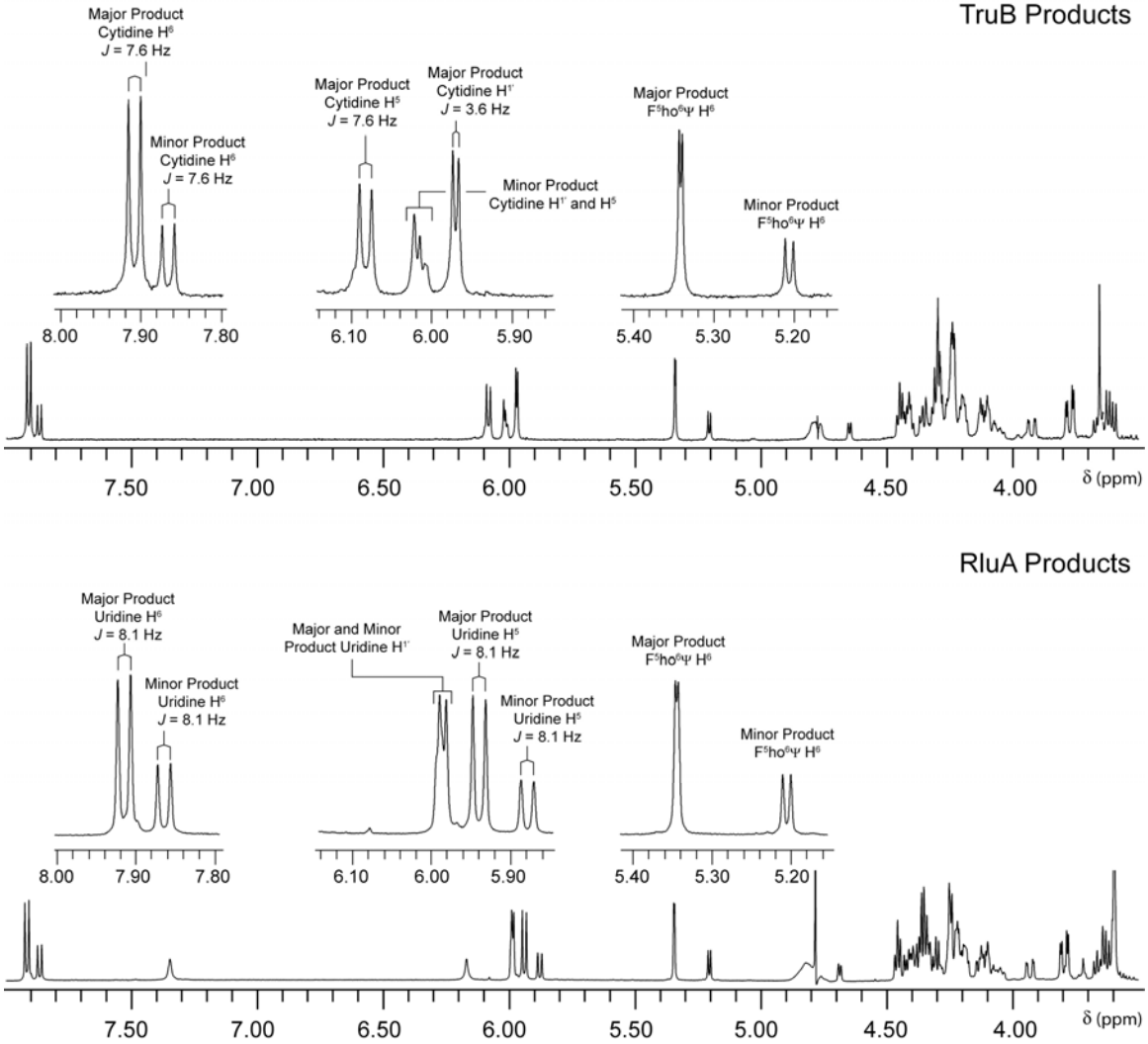

Figure 3. The ^{1}H NMR spectra of the dinucleotide products of F^{5}U in RNA from the action of TruB (*above*) and RluA (*below*). The 3′ nucleoside is either C or U, respectively, due to the difference in the sequences of the [F^{5}U]RNA.

The acquisition of spectral data for the mononucleotide product(s) of f^{5}U resulting from the action of RluA on stem-loop [f^{5}U]RNA if the dinucleotide product spectra are not definitive in establishing that they are the same as from the action of TruB.

The full suite of NMR experiments carried out on the products from RluA action, and in all cases, the results closely matched those for the products of TruB action (*e.g.*, Figure **4**), which indicates that the two enzymes almost surely generate the same products of F^{5}U and render the need to obtain mononucleotide products from the action of RluA.

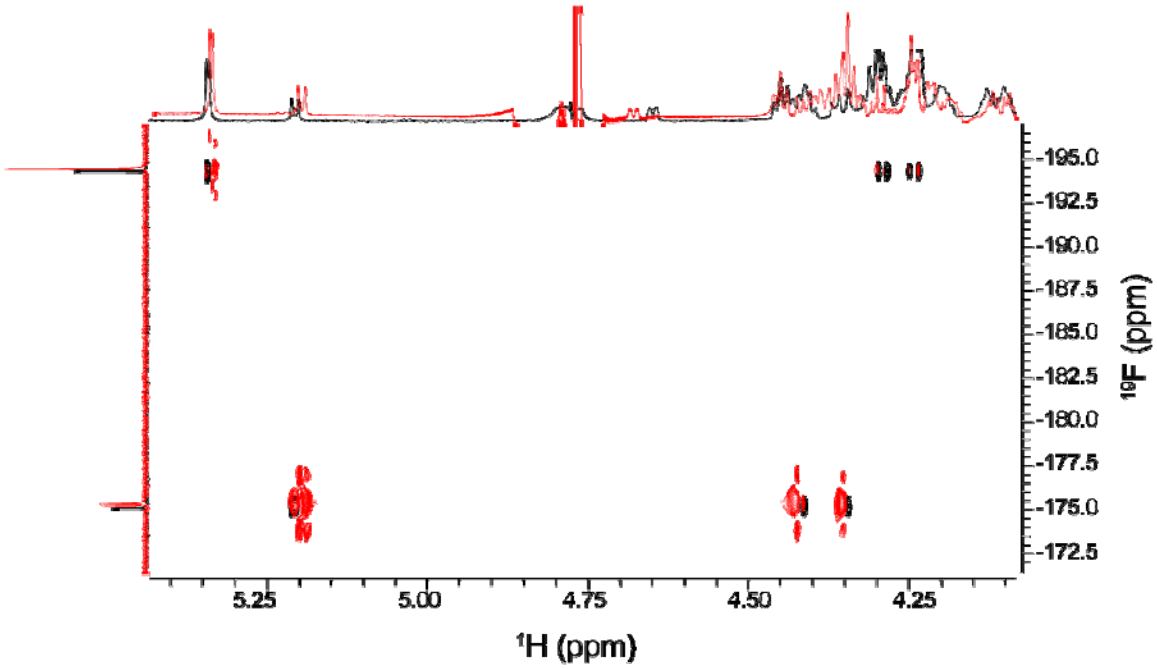

Figure 4. Overlay of the ^{1}H-^{19}F HSQC spectra of the dinucleotide products of F^{5}U in RNA from the action of TruB (*black*) and RluA (*red*).

Task 2. Devising new nanocomposites that can enhance wound healing (Dr. M. C. Yappert).

Year 1. Synthesize magnesia nanoparticles that effectively bind ATP and other polar compounds.
a. Sequential preparation of MgO/ATP nanocomposites.

Magnesia nanoparticles were synthesized using two different approaches:

i) Reaction of Mg acetate with NaOH, and
ii) Reaction of Mg ethoxide with water

The ratio of water to ethanol (or isopropanol) was varied from 1:0 (water only), to 1:0.25 to 1:0.50 and 1:0.75 and 0:1 (alcohol only). The addition of the reagents was performed in a conventional bath sonicator and also using a more powerful probe sonicator. The first reaction led to more aggregation.

Dynamic light scattering (DSL) studies were performed in all of the products to measure the particle size at different times after each reaction was completed. Both DLS and visual observations indicated, for all the reactions conducted, the presence of near μm size particles as well as larger (~10-μm diameter). To remove these large particles, centrifugation was performed. The fractions with the smaller nanoparticles (~100-nm diameter) were collected and analyzed by infrared (IR) spectroscopy. The amount of Mg in these fractions was measured (after digestion of the particles) by atomic absorption spectroscopy. Overall, the greatest yields of the smaller nanoparticles were observed for the products of reactions performed with the aid of the probe sonicator. However, these yields were not satisfactory (5% to 6%).

The temperature at which the reactions were carried out was also varied (25°C to 0°C) but it did not enhance the yields of the smaller particles. Faced with these difficulties, the preparation of the MgO/ATP nanocomposites was pursued with MgO nanopowder purchased from Sigma. The surface diameter and surface area reported by Sigma-Aldrich are < 50 nm and 130 m^2/g for the MgO nanopowder. The study of the interactions between the nanoparticles and ATP was performed by NMR spectroscopy and these results are going to be submitted as a manuscript during this month.

Reaction ii mentioned above was carried out in the presence of ATP in the aqueous solvent. The reaction product was allowed to settle overnight and then UV-vis and IR spectra were collected to determine the amount of ATP present in both the precipitate and the supernatant. The UV-vis traces showed a slight but reproducible shift in the absorption of ATP in the MgO/ATP nanocomposites relative to the ATP control. The presence of ATP led to a small improvement in the yield of the nanocomposites (5% to 7%), suggesting that ATP reduces the aggregation of the nanoparticles. Given the low yield of the reactions, the combined preparation of the nanohybrids, while feasible, is not going to be pursued.

B, Characterize interactions between MgO nanoparticles and ATP.
As the surface charge of metal oxide nanoparticles is affected by pH, we explored changes in ^{1}H and ^{31}P NMR chemical shifts of ATP-related resonances in aqueous solutions (pH: 4.2, 7.4 and 9.5) as the concentration of commercially available MgO nanoparticles was increased. The experimental trends indicate that the strongest interactions occur at physiological pH when the MgO nanoparticles are still positively charged and the □ phosphate group of ATP is undergoing its final deprotonation. Although the nanoparticles lead to the partial 'opening' of the 'self-stacked' form of ATP (at pH 7.4 and 9.5) in which the phosphates are stacked onto adenine, the major interactions with the MgO nanoparticles occur via direct attachment of the □ and □ phosphates.

Task 3 Characterization of the complex between Factor XIII and fibrinogen (Dr. M. C. Maurer).

Year 1. *E. coli* systems for expressing and purifying _C 242-424 will be optimized for producing the large amounts of isotopically labeled protein needed for NMR studies. We anticipate that both wild type and selected mutants will be desired for the studies. Unlabeled recombinant wild type FXIII A_2 and human derived FXIII B_2 will also be collected. Assessing NMR chemical shift assignments will begin.

Members of the coagulation cascade have far reaching effects on stemming blood loss, promoting wounding healing, and controlling heart disease, stroke, and arteriosclerosis. In the clotting process, thrombin cleaves off the N-terminal portions of the Aα and Bβ chains of fibrinogen $(A\alpha B\beta\gamma)_2$ to release FpA and FpB. The resultant fibrin monomers polymerize into ordered fibrin arrays. Activated Factor XIII (FXIII) is then responsible for catalyzing the formation of covalent crosslinks within the fibrin network and in fibrin-enzyme complexes. One of the binding sites for FXIII on fibrin has been found within αC 242-424, a segment located in the C-terminal portion of the fibrinogen Aα chain. The main objective of the current research is to examine in solution the structural and dynamic properties that govern interactions between FXIII and Fbg αC 242-424.

DNA for expressing Fbg αC 242-424 and FXIII A_2 in *Ecoli* have been obtained from collaborators. Strategies for expressing and purifying the resultant proteins have been developed and primers for required mutants have been designed. These approaches will now be implemented in the coming months. It will be important to

verify that the expressed FXIII A_2 is active and that the Fbg αC 242-424 can serve as an effective transglutaminase substrate. A kinetic assay that utilizes MALDI-TOF mass spectrometry for detecting loss of substrate and gain of product has been optimized. For the larger substrate Fbg αC 242-424, we will need to proteolytically digest the quenched kinetic samples with chymotrypsin prior to MALDI analysis. Some of the NMR studies will involve mapping interactions between FXIII subunits and Fbg αC 242-424. Amide proton hydrogen-deuterium exchange coupled with MALDI-TOF mass spectrometry (HDX-MS) is a complementary method to probe such interactions. Moreover, HDX-MS can be very helpful for examining protein regions where NMR chemical shifts cannot be assigned. We have collected data on the conformational effects that FXIII A_2 undergoes in the presence of different monovalent and divalent cations. Further knowledge has thus been gained on solution environments that can activate the transglutaminase and the structural consequences. The new information being collected on these different biophysical and kinetic sub-projects may aid in the design of new therapeutic agents to control blood loss and/or wound healing.

During the past quarter, further work has been carried out on setting up the expression system for Fbg αC 242-424 in Ecoli. Lab members have been trained in the required molecular biology methods and initial stages of the research work have taken place. A system which will subsequently be used to purify the expressed protein has been established. Further progress has also been made in using HPLC methods to follow activation of intact FXIII A_2. Some of the proposed NMR studies will involve mapping interactions between FXIII subunits and Fbg αC 242-424. Amide proton hydrogen-deuterium exchange coupled with MALDI-TOF mass spectrometry (HDX-MS) is a complementary method to probe such interactions. Further results have been obtained on FXIII regions that become exposed upon activation and are likely available for interactions with other proteins. Such information will become valuable for subsequent NMR studies on Fbg αC 242-424 and its responses to the introduction of FXIII A_2.

Task 4

d. Tensile properties of fibrous proteins (Dr. R. J. Wittebort)

Year 1: Complete 13C, 2H and 17O NMR of elastin to test hypothesis I. Publish results on elastin's mechanism of elasticity. Express and purify collagen constructs.

Our year 1 milestones includes three goals: (i) complete ^{13}C, ^{2}H and ^{17}O NMR of elastin to test hypothesis I, (ii) publish results on elastin's mechanism of elasticity and to (iii) express collagen constructs. In this 3rd-quarter, year-1 report the following significant Progress toward these milestones.

Regarding (i), two probes have been constructed and tested (shown in the first two panels of figure below) for executing the ^{13}C, ^{2}H and ^{17}O NMR experiments on the 500 MHz instrument. These probes have excellent sensitivity and are adapted for variable temperature experiments (see installed sample dewar in the 2nd panel below).

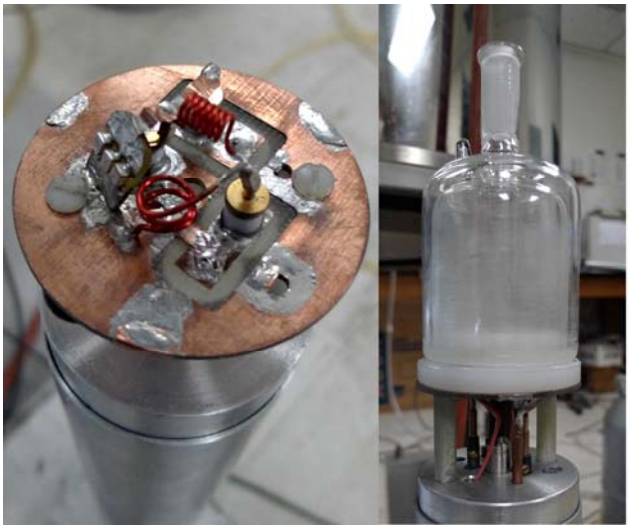

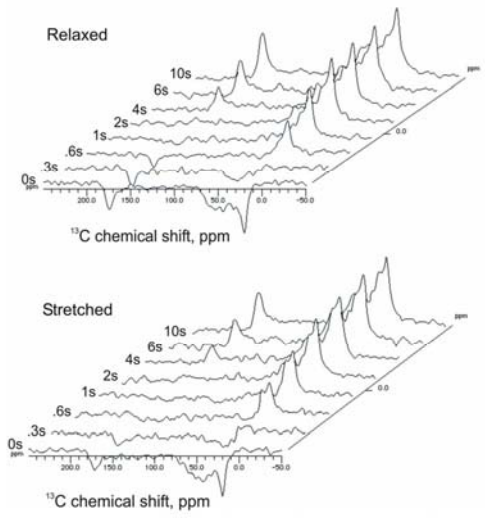

^{13}C relaxation data collected from elastin using this equipment is shown in the 3rd panel and summarized below.

site	T1 Stretched sec.	Relaxed
CO	5.3±0.8	4.1±.4
Ca	1.29±.22	1.20±.14
CH_3	0.53±.04	0.52±.03

Variable temperature ^{17}O spectra of non-stretched elastic fibers equilibrated against $H_2{}^{17}O$, not shown, display significant inhomogeneous line broadening resulting from protein:solvent interactions. Together, these data show that dynamics of the elastin chain vary little with stretch, however, elastin significantly perturbs the rotational dynamics of the surface water.

The effect of inhomogeneous line broadening in the O^{17} experiments is now being investigated in detail using multiple-quantum NMR. We have developed a suite of programs to optimize and interpret results from these experiments. Examples of an experiment for optimizing the detection of these spectra are shown below.

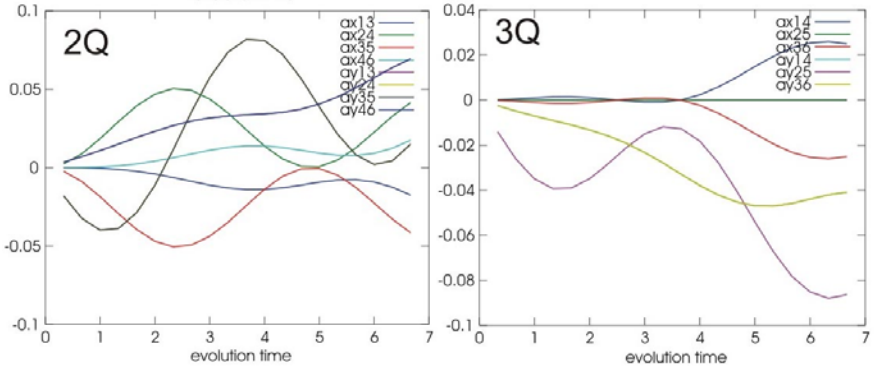

Specifically, we will measure solvent double (2Q) and triple (3Q) coherences to determine the amount of ordered water and the degree that it is ordered as a function of stretch. This, along with measurement of field-dependent ^{13}C relaxation dispersion, will complete these studies for publication (goal ii). This will be done during the 4th-quarter of year-1. The latter will become possible after completion of the 700 MHz instrument installation. At the time the instrument was purchased, installation during 12/09 was promised, however, the manufacturer has imposed significant delays and completion during 8/10 seems possible.

For goal iii (expression of heterotrimeric collagen fibers) we are collaborating with Professor Ron Koder (dept. of physics, CUNY). Ron's lab has expressed 22 proteins in the past two years and previously helped us express a 46-residue collagen fragment. The plasmid genes coding these constructs are being prepared commercially and Ron's group will guide us in transforming an expression strain of *e-coli.*

During the final quarter of year one, efforts were focused on two aspects of this project: (i) refining pulse sequences for sensitive and accurate acquisition of ^{2}H and ^{17}O double quantum spectra of elastin and (ii) design and preliminary construction of the triple resonance MAS probe.
With regard to (i), we can now collect high quality spectra that rigorously separate 2Q and 1Q signals using a combination 2Q filtration and two-dimensional (2D) separation of the 1Q and 2Q signals. High quality spectra are obtained with small elastin samples (5-10 mg) in three minutes of acquisition time. An example, collected on a fully hydrated elastin sample is shown below. Although the spectra are 2Q filtered, a small 1Q signal is still observed. In general, the 1Q:2Q signal ratio is not known and could easily be 100:1 or larger in these fully hydrated elastin samples. In our hands, 2Q filtration has a 50-fold rejection of the 1Q signal, so we devised an efficient 2-dimensional experiment that separates the residual 1Q signal from the desired 2Q signal in the indirect frequency dimension.

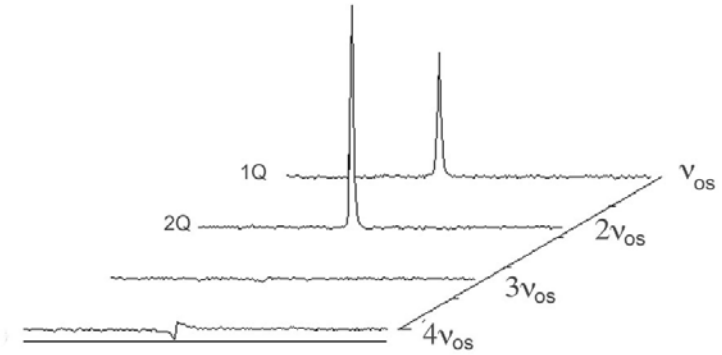

The experiment uses a constant time evolution period for the indirect dimension that separates the 1Q and 2Q signals on the basis of their different dependence on the offset frequency. Consequently, only 8 time increments in the indirect dimension are required to separate the 1Q signal and the entire 2Q signal appears in a signal slice. Thus, there is no S/N disadvantage relative to a 1D experiment and the 2Q signal intensity is unambiguously observed.

The DQ signal results from waters that are ordered, i.e., waters that are not isotropically reorienting and have lower entropy because of interaction with the matrix of the elastic protein. Our fundamental question is to determine to what extent does lower entropy "surface" water contribute to the entropy driven recoil of elastin. To do this, we will measure both changes in the amount of ordered water and the degree of water ordering as functions of elastin stretch and hydration. In our experiment, the amount of ordered water is proportional to the 2Q signal intensity and the degree of ordering is proportional to the residual quadrupole coupling, $\overline{\omega}_q$. The coupling is determined from the t-dependence of the 2Q signal intensity, $\sin(\overline{\omega}_q \tau)e^{-\tau/T_{2,2Q}}$, in the 2Q preparation period of the 2D experiment. This t-dependence is shown in the graph below.

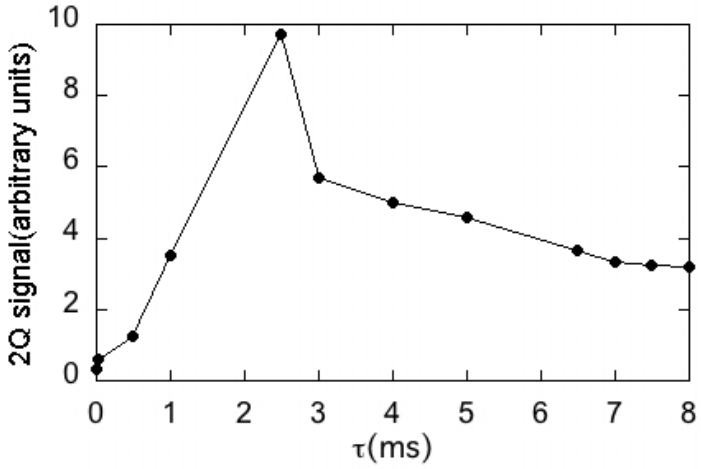

The pulse sequence also allows us to independently measure $T_{2,2Q}$. Thus, determining $\overline{\omega}_q$ from the above data amounts to a single parameter fit. Preliminary inspection of the data indicates that $\overline{\omega}_q / 2\pi \approx 100$ Hz.

In the next quarter, our probe and pulse sequence will allow us to make extensive measurements on the stretch and hydration dependence of water ordering in elastin. We expect that our approach is unique with regard to sensitivity, the ability to rigorously eliminate interference from 1Q signals and the use of NMR signals from both ^2H_2O and $H_2{}^{17}O$.

Regarding (ii), construction of the 1H/13C/15N triple resonance probe, an undergraduate honors student worked productively over the summer. He derived relevant design equation for the RF circuit, bread boarded the circuit, modified our probe tuning instrument for operation at 700 MHz, and confirmed that the design circuit can be tuned to the three NMR frequencies. Design equations are summarized in the table below.

Description	Nucleus	Tune	Match
Parallel resonant, Series C_m Match	13C/15N	$\omega^2 L = \frac{1}{(C_m + C_t)}$	$\frac{1}{\omega C_m} = \frac{Z_o \omega L}{R}$
Series Resonant, Parallel C_m Match	1H	$\omega^2 L = \frac{1}{C_t} + \frac{1}{C_m}$	$\frac{1}{\omega C_m} = \sqrt{R Z_0}$
Series Resonant, Parallel L_m Match	1H	$\omega^2 (L_m + L) = \frac{1}{C_t}$	$\omega L_m = \sqrt{R Z_0}$

In the above, L and C_t are the sample inductor and resonant capacitor, respectively. Subsequently, the student produced compact circuit boards for testing the probe in the 700 MHz magnet and is now preparing the complete mechanical design which contains a novel and more accurate mechanical apparatus for adjusting the magic angle. Overall, the probe is a triple resonance implementation of the highly efficient circuit used in the elastin studies. Consequently, we expect it to be similarly effective.

KEY RESEARCH ACCOMPLISHMENTS:

Task 1. We overexpressed the active C-terminal domain of enzyme ThiI, required for 4-thiouridine modification of tRNA. The two psuedouridine synthetases, TruB and RluA convert uridine to pseudourine in tRNA. We show the two enzymes generate the same products of F^5U.

Task 2. Nanoparticles of MgO were synthesized and their interactions with ATP were characterized.

Task 3. Set up an expression system for Fbg αC 242-424 in Ecoli. A protocol for purification has been determined.

Task 4. NMR probes for elastin spectroscopy built and tested. An expression system for heterodimeric collagen has been established. The entropy of water molecules on the surface of elastin has been measured.

REPORTABLE OUTCOMES:

Research

Jadhav, MA; Isetti, G; Trumbo, TA, and Maurer, M.C. Effects of Introducing Fibrinogen A alpha Character into the Factor XIII Activation Peptide Segment *Biochemistry*, **49:** 2918-2924 (2010).

Nyunt, MT; Dicus, CW; Cui, YY, Yappert, MC, Huser, TR, Nantz, MN and Wu, J.
Physico-Chemical Characterization of Polylipid Nanoparticles for Gene Delivery to the Liver
Bioconj. Chem.: **20,** 2047-2054 (2009).

Presentations

Patents
none

Conclusions

During the period covered by this report, a Request for Proposals was issued for instrumentation that was required for the successful conduct of the research described. The bids from Bruker and Varian were analyzed and it was decided to purchase a 400 MHz NMR, a 700 MHz NMR and a small-molecule x-ray diffractometer from Varian. These were installed and tested have recently become fully operational. In a parallel effort, the four research labs have been working toward the goal of utilizing these instruments for their specific projects. For Task 1, led by Professor Mueller, the active C-terminal domain of enzyme ThiI, required for 4-thiouridine modification of tRNA was overexpressed and can be prepared for NMR data acquisition. The two mononucleotide products of F^5U obtained from the action of TruB will now be rerun on the 700 HHz NMR to strengthen the conclusion that the two products are constrained conformers. For Task 2, led by Professor Yappert, characterization of the synthesized MgO nanopartle interaction with ATP has been accomplished by NMR, indicating a direct interaction. This is important if these compounds are to be useful in wound healing. Task 3, led by Professor Maurer, has developed the expression systems for the relevant portions of Factor XIII and fibrinogen and, with the spectrometers in place, characterization of this key interaction in the blood clotting cascade can be elucidated. Task 4, led by Professor Wittebort, saw the expression of heterodimeric collagen fibers and an expression system for a 46-residue collagen fragment is being readied. Concurrently, two NMR solid-state probes have been constructed and NMR studies are being performed to show the degree of water structuring as a driving for the tensile strength and elasticity of these fibers.

References

Jadhav, MA; Isetti, G; Trumbo, TA, and Maurer, M.C. Effects of Introducing Fibrinogen A alpha Character into the Factor XIII Activation Peptide Segment *Biochemistry*, **49:** 2918-2924 (2010).

Marley, J., Lu, M and Bracken, C. *J. Biomol. NMR,*, *20*, 71-75 . (2001).

Nyunt, MT; Dicus, CW; Cui, YY, Yappert, MC, Huser, TR, Nantz, MN and Wu, J.
Physico-Chemical Characterization of Polylipid Nanoparticles for Gene Delivery to the Liver
Bioconj. Chem.: **20,** 2047-2054 (2009).

Physico-Chemical Characterization of Polylipid Nanoparticles for Gene Delivery to the Liver

Maung T. Nyunt,[†] Christopher W. Dicus,[‡] Yi-Yao Cui,[§] M. Cecilia Yappert,[||] Thomas R. Huser,[†] Michael H. Nantz,[||] and Jian Wu*[,§]

NSF Center for Biophotonics Science and Technology, and Department of Internal Medicine, Transplant Research Program, University of California, Davis Medical Center, Sacramento, California 95817, Department of Chemistry, University of California, Davis, California 95616, and Department of Chemistry, University of Louisville, Louisville, Kentucky 40292.
Received April 3, 2009; Revised Manuscript Received October 1, 2009

Polylipid nanoparticles (PLNP) have been shown to be very effective in delivering antioxidative genes in the treatment of liver injury in mice. To build on our previous studies and to further characterize PLNP formulated from polycationic lipid (PCL) and cholesterol, we report here the synthesis of multigram quantities of PCL and employ analytical tools, such as Raman spectroscopy of single PLNP and live-cell imaging of lipofection, for the physicochemical characterization of PCL, PLNP, and the transfection process. Mass spectrometry demonstrates the characteristics of polymeric lipids. Raman spectrum of PCL reveals the polymeric structure of the polymers. The presence of cholesterol in PLNP formulation did not markedly change the Raman spectrum. PLNP-derived polyplexes exhibit Raman spectra very similar to PLNP except that the C−H out-of-plane deformation mode of the polymeric lipid is significantly suppressed, indicating the interaction with plasmid DNA. Zeta potential measurement indicates a large DNA-carrying capacity of PLNP and their stability for *in vivo* gene delivery. The live-cell fluorescent imaging dynamically shows that PLNP exerts transfection efficiency similar to lipofectamine in leading to early reporter gene expression in live hepatic cells. In conclusion, polylipid nanoparticles possess a high DNA carrying capacity and lipofection efficiency, rendering them suitable for testing in large animals. The employment of novel state-of-the-art technologies in the study of lipofection represents the level of physicochemical and biological characterization that is needed to best understand the key elements involved in the lipofection process.

INTRODUCTION

Lipid nanoparticles (LNP) have been used widely for *in vitro* gene delivery; however, their potential for *in vivo* gene delivery has been hampered by stability issues in the bloodstream, poor targeting efficiency, and transient transfection efficacy (*1*). Polylipid nanoparticles (PLNP), formulated from polycationic lipid (PCL) and cholesterol, on the other hand, have been documented to be more stable than DOTAP-DOPE[1]or DOTAP-cholesterol formulations in the bloodstream (*2*). We have also shown that PLNP-derived polyplexes were effective in delivering reporter genes, human antioxidative genes (extracellular superoxide dismutase (EC-SOD) or catalase) to the liver for the treatment of acute liver injury caused by hepatotoxins, or an ischemia/reperfusion procedure in two separate preclinical model systems (*3, 4*). These studies suggest that PLNP are a very effective gene transfer agent for liver-based delivery and have great potential to move from small animals to large animal trials as a step toward clinical applications (*5*). To develop an even more biocompatible gene delivery agent and to move this antioxidative gene approach from "bench to bedside", in-depth characterization of PCL, PLNP, and polyplexes, as well as feasible technologies for larger-scale synthesis of PCL, are needed. In this study, we employ state-of-the-art technologies, such as Raman microspectroscopy, mass spectrometry, and DeltaVision deconvolution microscopy (DVDM) for live cell imaging together with zeta potential measurements to further characterize PCL, PLNP, and PLNP-derived polyplexes. These novel technologies enable us to characterize the physicochemical features of PCL, PLNP, and PLNP-derived polyplexes, as well as the lipofection process, and further determine the stability of the polyplexes. We also describe modifications to our original method of PCL synthesis that enable multigram preparations of PCL sufficient for large animal experiments.

EXPERIMENTAL PROCEDURES

Synthesis of PCL. *Synthetic Procedures and Validation.* PCL (**1**) was prepared according to the synthetic route outlined in Figure 1. Prior to use, CH_2Cl_2 was immediately distilled from CaH_2. After reaction workup, solutions were dried using Na_2SO_4, and solvents were subsequently removed by rotary evaporation. Nuclear magnetic resonance (NMR) spectra were recorded with a General Electric QE-300 spectrometer (^{1}H at 300 MHz, ^{13}C at 75 MHz). Infrared spectra were recorded on a Mattson Genesis II FTIR 3000 spectrometer. Melting points are uncor-

* All correspondence should be addressed to Jian Wu, MD, PhD, Department of Internal Medicine, Transplant Research Program, UC Davis Medical Center, 4635 2nd Ave. Suite 1001, Sacramento, CA 95817, Tel. (916) 734-8044, Fax: (916) 734-8097, E-mail: jdwu@ucdavis.edu. Michael H. Nantz, PhD, Department of Chemistry, University of Louisville, Louisville, KY 40292, Tel. (502) 852-8069, Fax: (502) 852-8149, E-mail: mhnant01@louisville.edu.

[†] NSF Center for Biophotonics Science and Technology, University of California, Davis Medical Center.

[‡] Department of Chemistry, University of California, Davis.

[§] Department of Internal Medicine, Transplant Research Program, University of California, Davis Medical Center.

[||] Department of Chemistry, University of Louisville.

[1]Abbreviations: DOPE, L-α dioleoyl phosphatidylethanolamine; DOTAP, 1,2-bis(dioleoyloxy)-3-(trimethylammonio)propane; LNP, lipid nanoparticle; PCL, poly(cationic lipid); NMR, nuclear magnetic resonance; PLNP, polylipid nanoparticles; DVDM, DeltaVision deconvolution microscope.

10.1021/bc900150v CCC: $40.75
Published on Web 10/27/2009

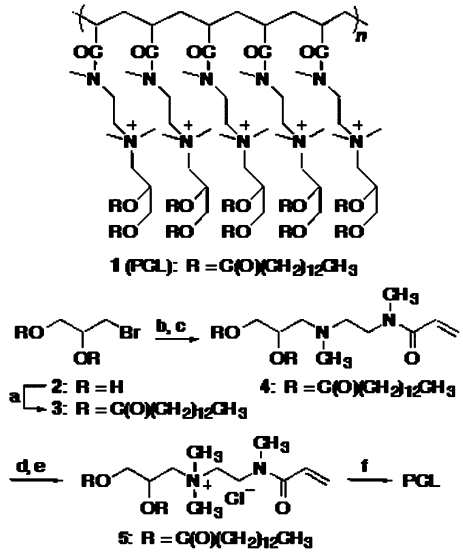

Figure 1. PCL synthetic route: (a) myristoyl chloride (2.5 equiv), Et_3N, cat. DMAP, CH_2Cl_2, 0 °C to rt, 3 h, 92%; (b) *N,N′*-dimethylethylenediamine (8 equiv), DMF, 70 °C, 45 min; (c) acryloyl chloride (1.5 equiv), Et_3N, CH_2Cl_2, 0 °C - rt, 2 h, 32% (2 steps); (d) CH_3I, rt, 18 h; (e) DOWEX 1 × 8−400, CH_2Cl_2/MeOH (9:1), 92% (2 steps); (f) *n*-dodecyl mercaptan (0.34 equiv), AAPH (0.1 equiv), H_2O, 80 °C, 15 h, 97%.

rected. Elemental analyses were performed by Midwest Microlabs (Indianapolis, IN). All sonications were performed in a bath sonicator (Laboratory Supplies Inc., Hicksville, NY).

*3-Bromo-1,2-bis(tetradecanoyloxy)propane (**3**).* To a solution of 3-bromo-1,2-propane-diol (**2**) (9.20 g, 59.4 mmol) in CH_2Cl_2 (50 mL) were added triethylamine (16.5 mL, 119 mmol) and 4-(*N,N*-dimethylamino)pyridine (400 mg). The reaction mixture was cooled to 0 °C, and then myristoyl chloride (40.4 mL, 149 mmol) was added dropwise. The reaction was warmed to room temperature and quenched after 4 h by pouring over saturated aqueous $NaHCO_3$ (100 mL). The aqueous layer was separated and the organic layer was washed successively with saturated aqueous $NaHCO_3$, water, and brine, and then dried (Na_2SO_4). The solvents were concentrated in vacuum, the crude residue was dissolved in ethanol, and minimal water was added to provide a cloudy suspension. The solution was placed in the freezer overnight causing bromodiester **3** to precipitate as a white solid (31.4 g, 54.6 mmol, 92%); mp 40−41.5 °C; IR (neat) 2913, 2848, 1731 cm^{-1}; ^1H NMR ($CDCl_3$) δ 0.85 (t, J = 6.6 Hz, 6H), 1.23 (m, 40H), 1.59 (m, 4H), 2.29 (m, 4H), 3.48 (m, 2H), 4.21 (dd, J = 11.9, 5.6 Hz, 1H), 4.30 (dd, J = 11.9, 4.4 Hz, 1H), 5.18 (m, 1H); ^{13}C NMR ($CDCl_3$) δ 14.0, 22.6, 24.8, 29.0−29.8 (6 signals), 31.9, 33.9−34.1 (3 signals), 62.9, 69.9, 172.6, 173.0; Anal. Calcd for $C_{31}H_{59}O_4Br$: C, 64.68; H, 10.33. Found: C, 64.75; H, 10.32.

*3-(N-Methyl-N-(2-N′-acrylamide-N′-methylamino)ethyl)amino)-1,2-bis(tetradecanoyl-oxy)propane (**4**).* To a solution of bromo diester **3** (23.9 g, 42.8 mmol) in *N,N*-dimethylformamide (200 mL) was added *N,N′*-dimethylethylenediamine (DMF) (36.8 mL, 342 mmol) via a syringe. The reaction was stirred under an argon atmosphere at 70 °C. After stirring 45 min, DMF and the unreacted diamine were removed by vacuum distillation. The residue was suspended in CH_2Cl_2 (250 mL) and washed successively with saturated aqueous $NaHCO_3$, water, and brine, and then dried (Na_2SO_4). The solvent was removed, and the crude product was passed through a short column of silica gel, eluting with 15% MeOH/CH_2Cl_2, to afford the crude diamino diester as yellow oil (9.6 g).

To a solution of the crude diamino diester (9.6 g, 16.5 mmol) in CH_2Cl_2 (100 mL) at 0 °C were added triethylamine (2.3 mL, 16 mmol) and 4-(*N,N*-dimethylamino)pyridine (200 mg). Acryloyl chloride (1.6 mL, 25 mmol) was added dropwise to the resulting solution, and the reaction mixture was warmed to room temperature. After stirring 3 h, the reaction was quenched by pouring over saturated aqueous $NaHCO_3$. The layers were separated, and the organic layer was washed with water and brine, dried (Na_2SO_4), and then concentrated by rotary evaporation. The residue was purified by column chromatography (SiO_2), eluting with a 3:2 mixture of EtOAc/hexane, to give the diester acrylamide **4** as a light yellow oil (8.72 g, 13.7 mmol, 32%); IR (neat) 2921 2852, 1737, 1654, 1614 cm^{-1}; ^1H NMR ($CDCl_3$) δ 0.87 (t, J = 6.6 Hz, 6H), 1.25 (m, 40H), 1.59 (m, 4H), 2.30 (m, 7H), 2.57 (m, 4H), 3.00 (s, 1.5H)*, 3.09 (s, 1.5H)*, 3.41 (m, 1H)*, 3.50 (m, 1H)*, 4.06 (m, 1H), 4.30 (m, 1H), 5.15 (m, 1H), 5.67 (dd, J = 10.2, 2.10 Hz, 1 H), 6.30 (dd, J = 2.1, 16.8 Hz, 0.5 H)*, 6.32 (dd, J = 2.0, 16.7 Hz, 0.5 H)*, 6.60 (dd, J = 10.2, 16.8 Hz, 1H); ^{13}C NMR ($CDCl_3$) δ 13.9, 22.5, 24.7, 28.9−29.4 (5 signals), 31.7, 34.0, 34.2, 36.0, 42.7, 43.0, 45.8, 48.2, 55.3, 56.3, 57.6, 58.0, 63.4, 63.6, 69.0, 69.2, 127.4, 127.6, 166.0*, 166.3*, 172.9, 173.1. Anal. Calcd for $C_{38}H_{72}O_5N_2$: C, 71.65; H, 11.39; N 4.40. Found: C, 71.32; H, 11.47; N 4.35. (*signals arising from amide stereoisomers).

N-(2-(*N′*-Acryloyl-*N′*-methylamino)ethyl)-*N,N*-dimethyl-*N*-[2,3-bis(tetradecanoyloxy)] propanammonium chloride (**5**). Acrylamide **4** (8.68 g, 13.6 mmol) was dissolved in methyl iodide (25 mL) and stirred at room temperature. After stirring for 18 h, methyl iodide was removed using a stream of argon. The crude residue was purified by column chromatography (SiO_2), eluting with a 9:1 mixture of CH_2Cl_2/MeOH. The product then was passed through a column of Dowex 1 × 8−400 ion-exchange resin (∼70 g), eluting with MeOH, to give **5** as a white solid (8.63 g, 12.6 mmol, 92%); IR (neat) 3564, 3358, 2954, 2916, 2848, 1743 cm^{-1}; ^1H NMR ($CDCl_3$) δ 0.84 (t, J = 6.2 Hz, 6H), 1.22 (m, 40H), 1.54 (m, 4H), 2.28 (m, 4H), 3.27 (s, 3H), 3.38 (s, 3H), 3.41 (s, 3H), 3.88 (m 2H), 4.04 (m, 4H), 4.29 (d, J = 13.8 Hz, 1H), 4.47 (dd, J = 2.6, 11.6 Hz, 1H), 5.59 (m, 1H), 5.73 (dd, J = 1.5, 10.5 Hz, 1H), 6.29 (dd, J = 1.5, 16.5 Hz, 1 H), 6.57 (dd, J = 10.4, 16.7 Hz, 1H); ^{13}C NMR ($CDCl_3$) δ 13.9, 22.5, 24.6, 24.7, 29.0−29.5 (4 signals), 31.8, 33.8, 34.1, 36.1, 42.3, 51.9, 62.5, 63.3, 64.2, 66.0, 127.2, 128.5, 167.3, 172.5, 172.9.

*The Final Product, PCL (**1**).* Monomer **5** (4.32 g, 6.28 mmol) was suspended in nanopure water (400 mL) by sonication at 50 °C for 45 min. The resultant homogeneous suspension was degassed by bubbling a stream of nitrogen through the suspension for 20 min. The suspension then was heated to 80 °C and stirred vigorously while adding *n*-dodecyl mercaptan (432 mg, 2.13 mmol), followed by a solution of 2,2′-azobis(2-methylpropionamidine) dihydrochloride (AAPH) (175 mg in 45 mL H_2O, 0.645 mmol). The resulting mixture was stirred at 80 °C for 15 h, after which the reaction vessel was placed in a freezer overnight (−10 °C). After thawing at room temperature, the precipitated solids were filtered and washed successively with cold diethyl ether to remove trace mercaptan and then dried under vacuum to afford PCL (4.21 g, 97%) as a white solid with spectral characterization identical to that previously reported (*6*).

Mass Spectral Analysis of PCL. PCL (5 mg) was dissolved in 1 mL of isopropanol. Both a 0.17 M solution of *para*-nitroaniline (PNA) and a 0.5 M solution of 2,5-dihydroxybenzoic acid (DHB) were prepared in isopropanol and used as matrices. PNA has been used previously for the detection of phospholipids in positive- and negative-ion spectra (*7*). A 1 μL aliquot of the analytical solution was spotted in each of five different sample wells of a 100-spot stainless steel MALDI plate (Applied Biosystems, Foster City, CA). The matrix (1 μL) was then added on top of each sample spot (dried droplet method). After

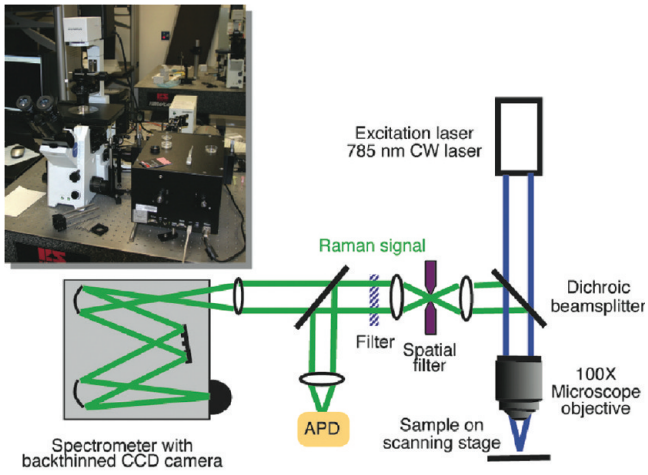

Figure 2. Schematic diagram of the Raman system combining a microscope, confocal detection system, and various laser sources. See the Methods and Materials part for details.

crystallization at ambient conditions, mass spectra were recorded on a Voyager Biospectrometry DE workstation (Applied Biosystems, Foster City, CA) equipped with a Nitrogen laser (λ = 337 nm). The extraction voltage was set to 20 kV. Mass spectra were acquired in both positive and negative modes.

Raman Micromicroscopy Analysis of PCL, PLNP, and PLNP-Derived Polyplexes. The Raman spectra of various LNP formulations were acquired using a Laser-Tweezers Raman microspectroscopy system, which is custom-built around a commercial inverted microscope platform (*8*). The main microscope frame consists of an Olympus IX-71 microscope, utilizing a 60×, NA 1.2, water immersion objective optimized for near-infrared operation. The laser source is an 80 mW, 785 nm diode-pumped solid-state laser, resulting in ~30 mW laser power in the microscope focus after passing multiple mirrors, a bandpass filter, and the microscope objective. The laser beam is focused to a diffraction-limited laser spot of ~500 nm diameter. The microscope is equipped with a mercury arc lamp for white-light fluorescence excitation through appropriate filters, as well as differential interference contrast for visualizing cells. Laser trapping and fluorescence excitation can be performed simultaneously. Spectroscopy is performed through an attached SP2300i spectrograph (Acton Research Corporation) and a back-illuminated thermoelectrically cooled deep-depletion CCD camera with 1340 × 1000 pixels (Figure 2).

The Use of a Fluorescence Deconvolution Microscopy System to Monitor the Lipofection Process. The automated fluorescence deconvolution microscopy system (*9*) (Personal DV, Applied Precision, LLC., Issaquah, WA) makes use of an Olympus IX-71 inverted optical microscope with a 250 W xenon illumination source, a 60× oil-immersion objective lens with a numerical aperture (NA) of 1.4 and a precision stepper-motor driven XYZ stage. The microscope is equipped with DAPI, FITC, TRITC, CY3, and CY5 filter sets, as well as 5 neutral density filters for the excitation source. It is capable of exciting fluorophores from the UV to the far-red and also collects transmitted light (bright field, differential interference contrast (DIC)) images. Image capture is achieved with a CoolSnap ES2 (Photometrics, Tucson, AZ)—a fast, high-resolution, high quantum efficiency, thermoelectrically cooled CCD camera. It can be used for both slow scan, high-resolution imaging of fixed samples or fast, high-sensitivity image capture of live cell samples.

The DeltaVision acquisition, image processing, and analysis software (*softWoRx 3.7.0*) run on a dual-processor personal computer running Cent OS Linux. The microscope is capable of separating up to 4 dyes and displaying triply labeled samples in a single image window through false colors. The DeltaVision software package automates the deconvolution computations, generates 3D reconstructions, and enables autofocusing, cell tracking, and live-cell imaging.

In our experiment, Hep G_2 cells were seeded on 35-mm-diameter round glass bottom culture dishes (MatTek Corp., Ashland, MA). The next day, cells were transfected with plasmid pEGFP-C1 by either PLNP or Lipofectamine, and then incubated at 37 °C. At specified time points, the culture dishes were mounted on the DeltaVision Deconvolution microscope. The temperature of the microscope stage was kept constant at 37 °C using an air-stream incubator (ASI-400, NevTek, Williamsburg, VA). GFP fluorescence of Hep G_2 cells was detected using a standard FITC filter set and corresponding bright field images were also collected. A series of images at different vertical focus positions resulting in optical sections (step size 0.1 μm) were captured with an image size of 512 by 512 pixels and setting binning to 2 × 2. The exposure time of between 0.1 to 0.3 s was sufficient to obtain images suitable for the dynamic range of the cooled CCD camera. Images were saved and processed using the DeltaVision software package (*softWoRx 3.7.0*) and Adobe Photoshop CS3.

Zeta Potential of PCL, PLNP, and Polyplexes. PLNPs were generated as reported previously and complexed with plasmid DNA at different charge ratios. The size distribution was determined by laser light scattering as reported previously (*10*). PLNPs or polyplexes in 2 μL were suspended in 2.5 mL water, and their zeta potentials were determined at room temperature in a Zeta Potential/Particle Sizer Nicomp 280 ZCS PSS-Nicomp Particle Sizing System (Santa Barbara, CA).

Statistical Analysis. The data of zeta potential in different charge ratios were analyzed by one-way variance test followed by multiple comparisons between groups with Newman-Keuls test. A *p*-value of less than 0.05 was considered as statistically significant.

RESULTS

Synthesis of PCL in a Multigram Quantity. The PCL synthesis proceeded from commercially available diol **2** by bisesterification using myristoyl chloride. Subsequent bromide displacement by *N*,*N*′-dimethylethylenediamine followed by reaction of the crude adduct with acryloyl chloride gave acrylamide **4**. Amine quaternization followed by counterion exchange using an established procedure (*11*) afforded acrylamide **5** as the chloride salt. The polymerization of **5** was accomplished by heating a suspension of **5** in water (ca. 15 mM) to 80 °C and then adding *n*-dodecyl mercaptan (*12*) and the water-soluble free radical initiator 2,2′-azobis(2-methylpropionamidine) dihydrochloride (AAPH) (*13*). The delay in addition of *n*-dodecyl mercaptan until the formulation of lipid nanoparticle with **5** differs from our previous protocol (*6*) and helps minimize conjugate addition of the thiol to the acrylamide. All intermediate products were validated by NMR spectral analysis, and the final polymeric product was determined in both negative and positive modes by mass spectral analysis (MALDI-TOF MS). The strongest MALDI-TOF MS signals were obtained with the use of *para*-nitroaniline (PNA) as the matrix. Although no detectable peaks were obtained in the negative mode, strong signals with maximal intensity at m/z = 651.6 were observed in positive-ion spectra, consistent with a polymeric product derived from monomer **5** (Figure 3). The product arising from conjugate addition of dodecyl mercaptan to the acrylamide moiety of **5** was observed at m/z = 853.6. Thus, our modified synthetic method produced PCL in multigram quantities, which is essential for generating enough PLNP for experiments in large animals.

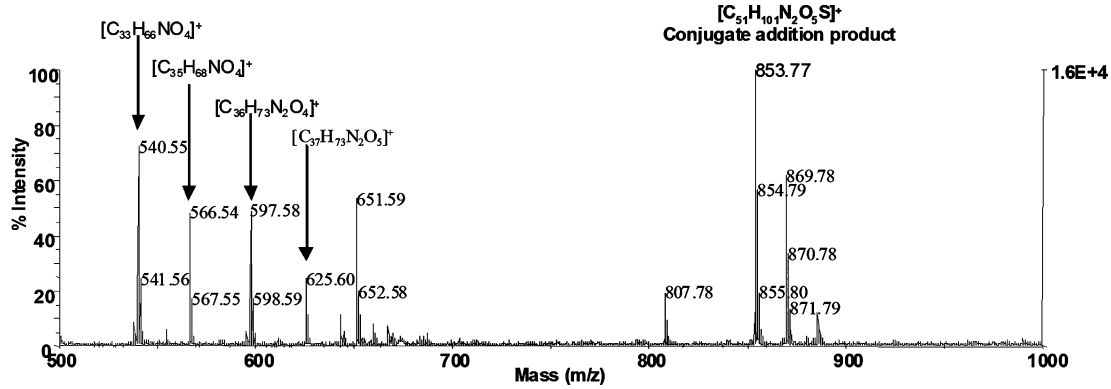

Figure 3. Mass spectral analysis of polycationic lipids. MALDI mass spectrum of PCL was obtained with the use of *para*-nitroaniline as the matrix. Mass spectra were recorded on a Voyager Biospectrometry DE workstation in both positive and negative modes. Strong signals with maximal intensity at $m/z = 651.6$ were observed in positive-ion spectra, indicating the product of polymerized cationic lipids (PCL).

Raman Spectroscopic Analysis of PCL, PLNP, and PLNP-Derived Polyplexes. We have obtained Raman spectra of the various starting materials at high concentration, such as plasmid DNA (3.6 μg/μL), pure lipofectamine, and pure cholesterol as received from the manufacturer, as well as unformulated PCL as synthesized (Figure 4A). For comparison, spectra of lipofectamine complexes with plasmid DNA (Figure 4B), as well as those of PCL vesicles, PLNP, and PLNP-derived polyplexes, were taken (Figure 4C). The Raman data from unformulated PCL are due to Raman scattering on carbon bonds, i.e., C−C, C═C, C−H, CH_2, and clearly show the polymeric nature of PCL (*14, 15*). The most prominent peaks are C−C stretch modes in the 1100−1200 cm^{-1} and the 1300 cm^{-1} range, and the 1445 cm^{-1} methylene bending vibration in the polymer. Similar features with less pronounced peaks besides the 1445 cm^{-1} methylene deformation mode were found for lipofectamine and cholesterol. Cholesterol contains an additional strong C═C vibration at ~1670 cm^{-1}. The spectrum of plasmid DNA (Figure 4A) is dominated by DNA marker modes such as the 785 cm^{-1} cytosine ring breathing vibration, the 1090 cm^{-1} vibration from the phosphate backbone, the abundant 1442 cm^{-1} CH mode, and the 1575 cm^{-1} adenine vibration (*16*). In addition, this spectrum contains contributions from the solvent (Tris-EDTA buffer) at 1060 cm^{-1}, as well as from polysaccharides from bacterial lysate at 860 cm^{-1} (*15, 17*). These endotoxins are, however, only present in this highly concentrated form of plasmid DNA, which was required to obtain its Raman spectrum. The DNA used for forming lipoplexes or polyplexes is free of endotoxins. The spectrum of lipofectamine remains unaltered upon dilution (data not shown). Lipofectamine-derived lipoplexes exhibit combined Raman peaks due to lipofectamine as well as DNA. Most noticeable are a weak 785 cm^{-1} cytosine breathing mode, the 1090 cm^{-1} vibration from the phosphate backbone, and the 1660 cm^{-1} amide I mode (Figure 4B). Raman spectra were acquired from individual optically trapped PCL, PLNPs, and PLNP polyplex vesicles within a 30 s signal integration time. Interestingly, PCL changes its spectrum between unformulated PCL and formulated PCL nanoparticles. Most notable is the addition of a strong 1001 cm^{-1} C−H out-of-plane deformation mode. C−H and C−C modes in this spectral range are known to be sensitive markers of acyl chain disorder (*8, 14*). This has been widely observed in lipid vesicles. On the basis of these observations, we attribute this strong peak to the increased chain disorder in formulated PCL when compared to unformulated PCL powder. Interestingly, the addition of cholesterol to PCL nanoparticles to form PLNP does not noticeably change the Raman spectrum of these particles, i.e., the disordered state of the polymer chains is retained in the presence of cholesterol. PLNP-derived polyplexes undergo a marked change in their Raman spectrum when compared to PLNP. Here, the 1001 cm^{-1} C−H out-of-plane deformation mode is significantly suppressed due to interaction with plasmid DNA. We attribute this to strong interactions of the charged DNA backbone with the charged polymer chains, which apparently leads to strong ordering in the vesicle chain structure (Figure 4C). The presence of DNA in polyplexes is further confirmed by the presence of weak DNA markers, such as the 785 cm^{-1} cytosine breathing mode, the 1090 cm^{-1} phosphate vibration, and the 1660 cm^{-1} amide I mode.

Use of Fluorescence Deconvolution Microscopy to Dynamically Monitor Reporter Gene Expression. To dynamically determine the earliest expression of a reporter gene, enhanced green fluorescent protein (GFP), we employed a fluorescence microscopy imaging system for time-elapsed live cell imaging to compare the transfection efficiency of PLNP with lipofectamine. As shown in Figure 5, the earliest GFP expression in Hep G_2 cells was seen 60 min after PLNP-mediated transfection with a pEGFP-C1-EGFP plasmid at the charge ratio of 5:1 (Figure 5A,D), while focal and faint GFP expression was also seen in Hep G_2 cells 70 min after lipofectamine transfection (Figure 5G,J), indicating that lipid nanoparticle-mediated plasmid DNA entering a cell and the nucleus, i.e., the transcription of the reporter gene, is a rather fast process. GFP expression then became more intense and spread throughout Hep G_2 cells transfected either with PLNP (Figure 5B,C,E,F) or lipofectamine (Figure 5H,I,K,L). This observation indicates that the transfection efficiency of PLNP is at least as good as lipofectamine in Hep G_2 cells.

Zeta Potential, Charge Ratios, Size, and Visualization of PLNP and Polyplexes. In order to further determine the relationship of charge ratios and zeta potential of PLNP and PLNP-derived polyplexes, we mixed PLNP with plasmid DNA at various charge ratios, and measured the zeta potential and size of PLNP and PLNP-derived polyplexes at the same time. It is clear from Figure 6 that, for *in vitro* transfection at a charge ratio of 5:1, the zeta potential of polyplexes was slightly lower than PLNP without DNA ($p > 0.05$). For *in vivo* gene delivery at the charge ratio of 1.25:1, the zeta potential of the polyplexes was negative (-6.46 ± 0.97 mV), which is consistent with them being less reactive to serum proteins as reported previously (*2*). We also noticed that the size of polyplexes increased when PLNP were complexed with plasmid DNA. The polyplex size was within the range 200−400 nm, which are similar to many other lipid formulations reported (*18, 19*). The stability of our PLNP was further confirmed *in vitro* when PCL and PLNP vesicles were prepared by sonication to result in nanoparticles with a diameter of 149 ± 62 nm. Under the microscope, we were able to visualize the vesicles of both PCL and PLNP by their absorption of transmitted light (highlighted by a circle) (Figure 7A). The vesicles appear homogeneous in size and

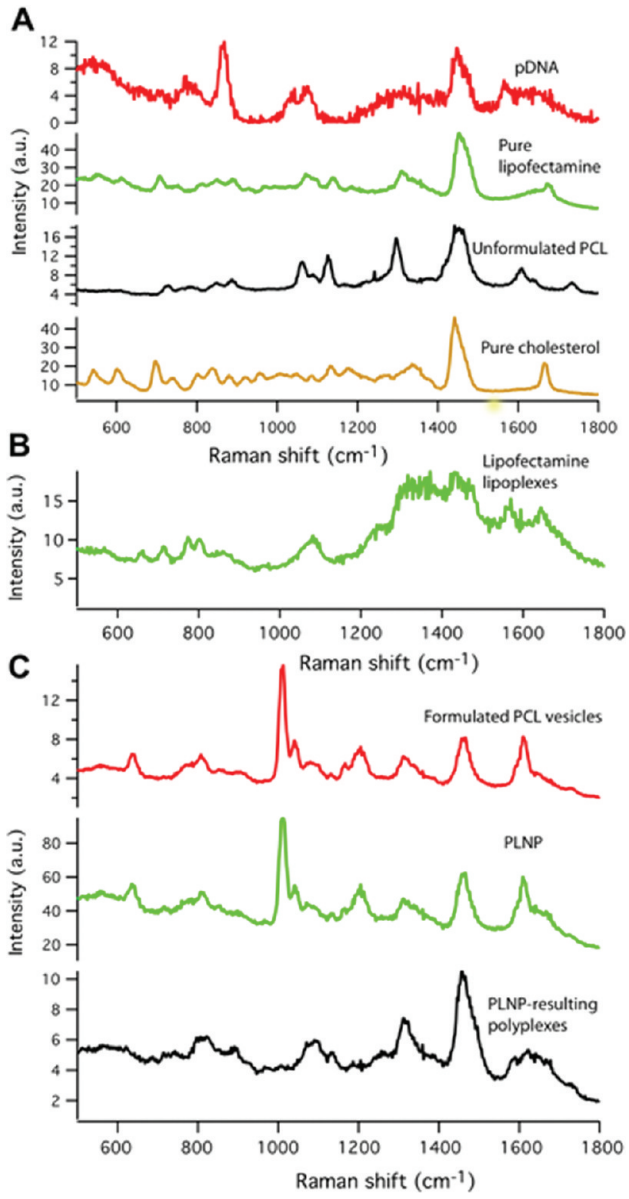

Figure 4. Representative Raman spectrum of pure compounds, nanoparticles, and lipoplexes or polyplexes. (A) Plasmid DNA (red), pure lipofectamine (green), unformulated PCL (black), and pure cholesterol (orange). (B) Lipofectamine-derived lipoplexes (green) in 30s signal integration time. (C) PCL vesicles (red), PLNP (green), and PLNP-derived polyplexes (black). The Raman spectrum was obtained in a Laser-Tweezers Raman microspectroscopy system, and representative spectrum is shown from each condition.

shape. The morphology of these particles did not change significantly after complexation with plasmid DNA (Figure 7B), whereas lipofectamine formed large aggregates in the presence of plasmid DNA (4 μL liposomes/2 μg DNA) (Figure 7C). These data indicate that our PLNP formulation is superior to lipofectamine in DNA binding capacity and particle stability when forming complexes with plasmid DNA.

DISCUSSION

In our previous study, a cationic acrylamide lipid was polymerized to form PCL (*6*). Our PLNP formulated from PCL and cholesterol have been considered as one of a few nonviral lipid nanoparticle formulations (*20, 21*) useful for *in vivo* gene transfer due to their nontoxic feature, high stability in the bloodstream, and superior transfection efficacy in mouse liver (*2, 6*). The preclinical proof-of-concept experiments in two separate model systems demonstrated that the delivery of antioxidative genes, either EC-SOD or catalase, or in combination, protected mouse from acute liver injury induced by hepatotoxins or hepatic ischemia/reperfusion procedures (*3, 4*). These studies were highlighted as "the basis for studies with larger animals and may help bridge the gap between the basic understanding of pathophysiologic processes in animal models towards a practical clinical application in liver transplantation" (*5*). In order to perform large animal experimentation, such as in pigs or nonhuman primates, or for clinical use, we developed a feasible synthetic route for synthesizing PCL on a relatively large scale. The purity of the final product with the polymeric features was verified by mass spectrometry; and PLNP were formulated with the final product and used in the experiments of this study.

Raman spectroscopy is a laser-based analytical technique that enables chemical characterization of molecules in microscopically small samples (*8*). Raman microspectroscopy is based on the inelastic scattering of photons by molecular bond vibrations and is a useful tool for the chemical analysis of lipids, lipoplexes, or polyplexes due to its ability to provide chemical group identification (*22*). A particular advantage of micro-Raman spectroscopy is its unrivaled sensitivity and its relative noninvasiveness, which enables the nondestructive analysis of nanoscopic compounds as small as 50 nm diameter (*8, 14*). We have employed Raman microspectral analysis in a number of studies (*23, 24*), including analyzing the chemical composition of individual triglyceride-rich lipoproteins (*25*). A Raman spectrum appears when a small portion of the photons from a monochromatic light source is scattered by interaction with the bonds resulting in a shift toward higher or lower frequencies. The energy difference between the incident and scattered photons corresponds to the vibrational energy of the specific molecular bond interrogated. A Raman spectrum obtained from lipids, DNA, or their complexes provides an intrinsic molecular fingerprint of these samples, and reveals characteristic information about macromolecular conformations (*8*). In order to further characterize the chemical features of PCL, PLNP, and PLNP-derived polyplexes, we employed a laser-tweezers Raman microspectroscopy system to observe morphologic changes in these particles after complexation with plasmid DNA and to acquire Raman spectra of polyplexes and compare them with lipofectamine lipoplexes. After carefully comparing with pure reagents for PLNP formulation and polyplex formation, we found that the Raman spectra of PCL exhibits polymeric characteristics of the synthetic polymer and that the spectra of PLNP indicate that they readily interacted with plasmid DNA and formed complexes without aggregation. Lipofectamine, on the other hand, was observed to form large aggregates devoid of specific interactions with DNA after complexation with plasmid DNA. These findings, which have not been reported, imply the feasibility of *in vivo* application of PLNP.

The appearance and extent of reporter gene expression in transfected cells are generally determined either by measuring activity of luciferase after lysing cells or by observing the onset of fluorescence from GFP expression at certain time points with a regular fluorescent microscope. It is generally believed that the lipofection process usually takes at least 6 h in transfected cells (*26*). In our previous experiments, we compared transfection efficiency in Hep G_2 cells between PLNP and lipofectamine by luciferase activity and cytotoxicity, and found that PLNP is less toxic than lipofectamine in primary hepatocytes and displayed transfection efficiency in Hep G_2 cells similar to lipofectamine (*6*). The automated fluorescence microscopy imaging system offers the possibility to dynamically monitor the transfection process in live cells, and we noticed that the earliest GFP appearance was within 1 h in Hep G_2 cells

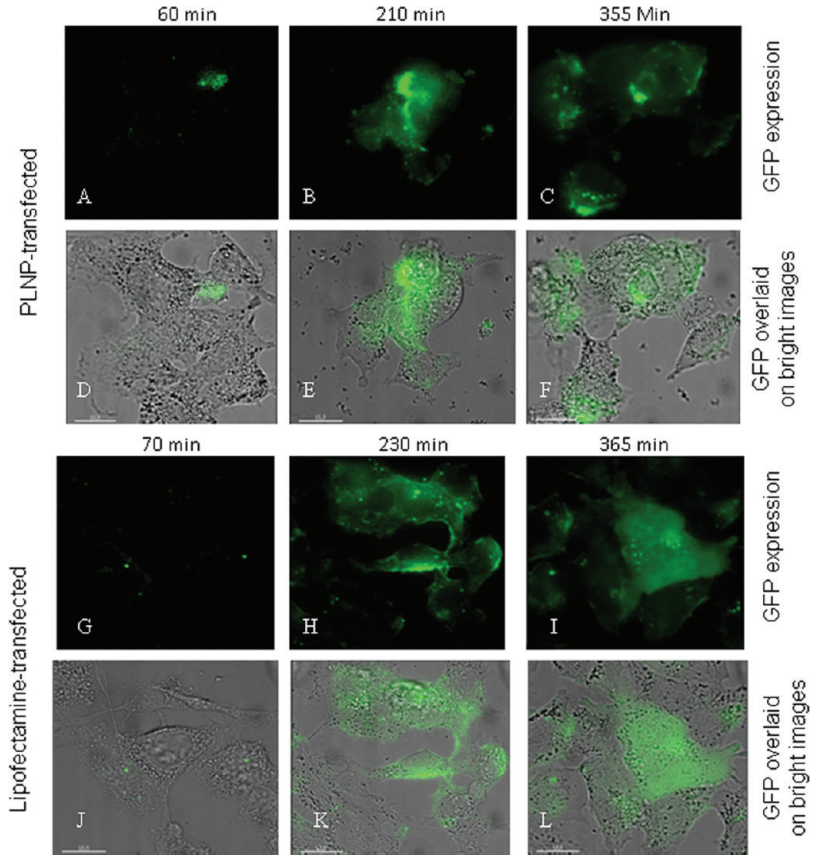

Figure 5. Representative vertical section images of automated fluorescence deconvolution microscopy examination of GFP expression in Hep G2 cells. After transfection, the culture well was mounted in the temperature-controlled platform. Image capture is achieved with a fast, high-resolution, high quantum efficiency, thermoelectrically cooled CCD camera at various time points as indicated. A, B, C and G, H, I representative images are selected from a stack of vertical section images of individual cells at indicated time points. C, D, E, and J, K, L are the overlaid images of A, B, C and G, H, I with their bright field images.

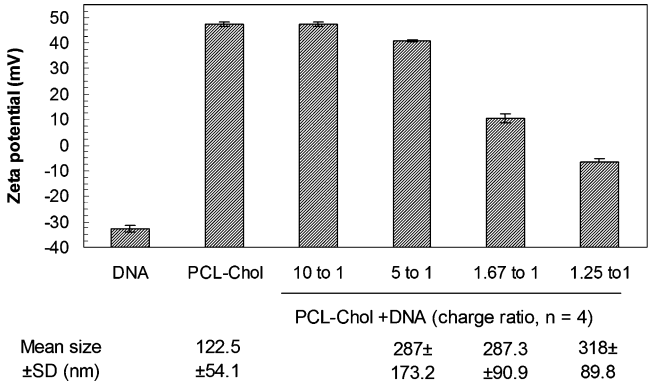

Figure 6. Zeta potential and size changes of PLNP formulation (PCL-Chol). The zeta potential and size were measured by a zeta potential/particle sizer at the charge ratios used for both *in vitro* and *in vivo* experiments ($n = 3$). It is found that the zeta potential was reduced to be neutral or even negative when the charge ratio was decreased to a range from 1.25 to 1, and that lipoplex size increased, but stayed within the 200−400 nm range.

transfected with PLNP, and a relatively faint GFP image was also seen in Hep G_2 cells transfected with lipofectamine 20 min later. Thereafter, the intensity and spread of GFP were similar in cells transfected by either PLNP or lipofectamine. Thus, we were able to dynamically monitor an early lipofection process in live cells over time. The time-lapsed imaging mode of the automated fluorescence deconvolution microscope minimizes long-term photobleaching by rapidly shuttering the excitation source on and off. The detection is based on a digital thermoelectrically cooled CCD camera, which enables us to quantitatively and dynamically determine GFP fluorescence (i.e., expression) levels in the cytoplasm over time. When specific dyes are used to indicate subcellular organelles, the DVDM system also allows detection of multiple, different-colored fluorescence signals simultaneously from cells with high sensitivity together with their morphology in three dimensions without damaging cells (*9*). The figure in Supporting Information is an example of this application. With this system, it is possible to investigate at a specific time point which subcellular organelles are involved in the lipofection process and critical events, such as intracellular trafficking of plasmid DNA, interaction, or synchronization of multiple subcellular organelles.

One of the critical features of cationic lipid, polymers, lipid nanoparticles, lipoplexes, or polyplexes is the zeta potential, which reflects charge force for nucleotide binding. Both size distribution and zeta potential may change after the formation of complexes with plasmid DNA. These two are important parameters of polyplex stability, and are even more critical when polyplexes are used for *in vivo* gene transfer. When forming polyplexes, the charge ratio will be a key factor affecting both zeta potential and transfection efficiency (*27*). A high zeta potential often benefits *in vitro* transfection, whereas neutral or negative zeta potential of lipoplexes or polyplexes may have less serum reactivity and is beneficial for complex stability in the bloodstream (*27, 28*). When similar transfection efficiency is reached, a lower charge ratio (positive charge from cationic lipid over negative charge in DNA) indicates that less cationic lipid is needed for maximal plasmid DNA binding, which indicates the carrying capacity of specific lipids. We have previously shown that our PLNP formulation exhibited similar transfection efficiency when the charge ratio was changed from

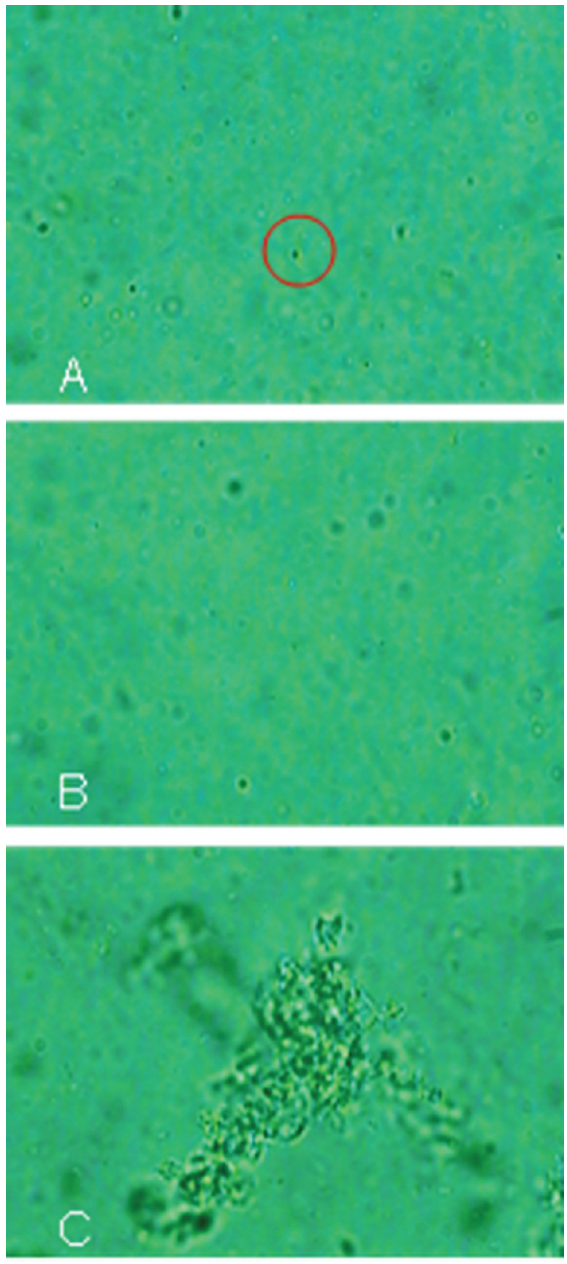

Figure 7. Visualization of lipid vesicles under a light microscope. (A) A PLNP vesicle was visualized under the microscope used for Raman spectromicroscopy analysis (600×), and it is marked with a circle. (B) Polyplexes derived from PLNP and plasmid DNA. (C) Lipoplexes derived from lipofectamine with plasmid DNA. The PLNP morphology of these particles did not change after complexation with plasmid DNA; however, lipofectamine formed large aggregates in the presence of plasmid DNA.

1:3 to 1:5, indicating higher DNA binding and carrying capacity of this formulation (*6*). In the present study, we found that the zeta potential was reduced to be neutral or even negative when the charge ratio was decreased to a range from 1.25 to 1, and the data indicate that this charge ratio is beneficial for *in vivo* delivery through intravenous administration because it may have less reactivity to negatively charged serum proteins. This is a key issue that is under-addressed in the field of lipofection. The net positive charge of polyplexes or lipoplexes is the principal reason for the formation of large aggregates after intravenous administration of lipoplexes or polyplexes and may affect tissue distribution and gene transfer efficacy in specific organs, such as livers when nonviral lipid nanoparticles are used as gene transfer vectors (*29*). The microscopic morphology of PLNP and polyplexes, as shown in Figure 7, further confirmed the stability after complexation with plasmid DNA, and there is a striking contrast to the formation of large aggregates of lipofectamine-derived lipoplexes. Therefore, our PLNP are useful for both *in vitro* and *in vivo* gene transfer as demonstrated in our previous studies and may also be useful in delivering siRNA, similar to other cationic lipid nanoparticles (*30*).

In summary, the employment of novel state-of-the-art technologies in the study of lipofection represents the level of physicochemical and biological characterization that is needed to best understand the key elements involved in the lipofection process. In the present study, we have described a refined method of PCL synthesis on a multigram scale. The data demonstrate that the morphology of PLNP derived from PCL did not change significantly after interaction with plasmid DNA, which is in striking contrast to the formation of large aggregates when using lipofectamine. The large DNA carrying capacity allows PLNP to be saturated with negatively charged plasmid DNA, and the negative zeta potential of PLNP-derived polyplexes is beneficial for *in vivo* stability. The Raman spectral signatures of PCL, PLNP, and polyplexes reflect the polymeric nature of PLNP and the close interaction of PLNP with plasmid DNA. These data are in concordance with the good stability observed for PLNP in the bloodstream and the higher transfection efficiency *in vivo* compared to other formulations of lipid nanoparticles.

ACKNOWLEDGMENT

We thank Mr. Souvik Biswas for his assistance in preparing samples for analysis. C.W.D. is grateful for the award of an R. Bryan Miller Fellowship from the UCD Department of Chemistry during the course of this study. This work was supported by grants from the NIH (DK069939) and the UCD Medical Center (Technology Transfer Grant to J.W.), from the National Science Foundation (to T.R.H.). The Center for Biophotonics, an NSF Science and Technology Center, is managed by the University of California, Davis, under Cooperative Agreement No. PHY 0120999. Part of the data was presented in the 11th Annual meeting of the American Society for Gene Therapy (ASGT), May 28−June 1, 2008, Boston, MA. Mr. Maung Nyunt received a travel award from the ASGT for the presentation.

Supporting Information Available: The use of the DVDM system enables us to section cells at 0.1 μm thicknesses, and a three-dimensional structure of a cell can be built from the sections at the *Z* axis. This material is available free of charge via the Internet at http://pubs.acs.org.

LITERATURE CITED

(1) Li, S. D., and Huang, L. (2006) Gene therapy progress and prospects: non-viral gene therapy by systemic delivery. *Gene Ther. 13*, 1313–9.
(2) Liu, L., Zern, M. A., Lizarzaburu, M. E., Nantz, M. H., and Wu, J. (2003) Poly(cationic lipid)-mediated in vivo gene delivery to mouse liver. *Gene Ther. 10*, 180–7.
(3) He, S. Q., Zhang, Y. H., Venugopal, S. K., Dicus, C. W., Perez, R. V., Ramsamooj, R., Nantz, M. H., Zern, M. A., and Wu, J. (2006) Delivery of antioxidative enzyme genes protects against ischemia/reperfusion-induced liver injury in mice. *Liver Transpl. 12*, 1869–79.
(4) Wu, J., Liu, L., Yen, R. D., Catana, A., Nantz, M. H., and Zern, M. A. (2004) Liposome-mediated extracellular superoxide dismutase gene delivery protects against acute liver injury in mice. *Hepatology 40*, 195–204.
(5) Luedde, T., and Trautwein, C. (2006) The role of oxidative stress and antioxidant treatment in liver surgery and transplantation. *Liver Transpl. 12*, 1733–5.

(6) Wu, J., Lizarzaburu, M. E., Kurth, M. J., Liu, L., Wege, H., Zern, M. A., and Nantz, M. H. (2001) Cationic lipid polymerization as a novel approach for constructing new DNA delivery agents. *Bioconjugate Chem. 12*, 251–7.

(7) Estrada, R., and Yappert, M. C. (2004) Alternative approaches for the detection of various phospholipid classes by matrix-assisted laser desorption/ionization time-of-flight mass spectrometry. *J Mass Spectrom. 39*, 412–22.

(8) Chan, J. W., Motton, D., Rutledge, J. C., Keim, N. L., and Huser, T. (2005) Raman spectroscopic analysis of biochemical changes in individual triglyceride-rich lipoproteins in the pre- and postprandial state. *Anal. Chem. 77*, 5870–6.

(9) Falk, M. M. (2000) Connexin-specific distribution within gap junctions revealed in living cells. *J. Cell Sci. 113*, 4109–20 (Pt 22).

(10) Wu, J., Liu, P., Zhu, J. L., Maddukuri, S., and Zern, M. A. (1998) Increased liver uptake of liposomes and improved targeting efficacy by labeling with asialofetuin in rodents. *Hepatology 27*, 772–8.

(11) Aberle, A. M., Bennett, M. J., Malone, R. W., and Nantz, M. H. (1996) The counterion influence on cationic lipid-mediated transfection of plasmid DNA. *Biochim. Biophys. Acta 1299*, 281–3.

(12) Madruga, E. L., San Roman, J., and Benedi, P. (1990) High conversion polymerization of methyl methacrylate in the presence of n-dodecylmercaptan. *J. Appl. Polym. Sci. 41*, 1133–1140.

(13) Dorn, K., Klingbiel, R. T., Specht, D. P., Tyminski, P. N., Ringsdorf, H., and O'Brien, D. F. (1984) Permeability characteristics of polymeric bilayer membranes from methacryloyl and butadiene lipids. *J. Am. Chem. Soc. 106*, 1627–1633.

(14) Chan, J., Fore, S., Wachsmann-Hogiu, S., and Huser, T. (2008) Raman spectroscopy and microscopy of individual cells and cellular components. *Laser Photon Rev. 2*, 325–334.

(15) Manoharan, R., Wang, Y., and Feld, M. S. (1996) Histochemical analysis of biological tissues using Raman spectroscopy. *Spectrochim. Acta, Part A 52*, 215–249.

(16) Huser, T., Orme, C., Hollars, C., Corzett, M., and Balhorn, R. (2009) Raman spectroscopy of DNA packaging in individual human sperm cells distinguishes normal from abnormal cells. *J. Biophotonics 2*, 322–332.

(17) Serban, D., Benevides, J. M., and Thomas, G. J. (2002) DNA secondary structure and Raman markers of supercoiling in Escherichia coli plasmid pUC19. *Biochemistry 41*, 847–853.

(18) Pelisek, J., Gaedtke, L., DeRouchey, J., Walker, G. F., Nikol, S., and Wagner, E. (2006) Optimized lipopolyplex formulations for gene transfer to human colon carcinoma cells under in vitro conditions. *J. Gene Med. 8*, 186–97.

(19) Almofti, M. R., Harashima, H., Shinohara, Y., Almofti, A., Baba, Y., and Kiwada, H. (2003) Cationic liposome-mediated gene delivery: biophysical study and mechanism of internalization. *Arch. Biochem. Biophys. 410*, 246–53.

(20) Elfinger, M., Uzgun, S., and Rudolph, C. (2008) Nanocarriers for gene delivery - polymer structure, targeting ligands and controlled-release devices. *Curr. Nanosci. 4*, 322–353.

(21) Ambegia, E., Ansell, S., Cullis, P., Heyes, J., Palmer, L., and MacLachlan, I. (2005) Stabilized plasmid-lipid particles containing PEG-diacylglycerols exhibit extended circulation lifetimes and tumor selective gene expression. *Biochim. Biophys. Acta 1669*, 155–63.

(22) Braun, C. S., Jas, G. S., Choosakoonkriang, S., Koe, G. S., Smith, J. G., and Middaugh, C. R. (2003) The structure of DNA within cationic lipid/DNA complexes. *Biophys. J. 84*, 1114–23.

(23) Wachsmann-Hogiu, S., Weeks, T., and Huser, T. (2009) Chemical analysis in vivo and in vitro by Raman spectroscopy-from single cells to humans. *Curr. Opin. Biotechnol. 20*, 1–11.

(24) Chan, J., Fore, S., Wachsmann-Hogiu, S., and Huser, T. (2008) Raman spectroscopy and microscopy of individual cells and cellular components. *Laser Photon Rev. 2*, 325–334.

(25) Chan, J. W., Motton, D., Rutledge, J. C., Keim, N. L., and Huser, T. (2005) Raman spectroscopic analysis of biochemical changes in individual triglyceride-rich lipoproteins in the pre- and postprandial state. *Anal. Chem. 77*, 5870–6.

(26) Lang, I., Scholz, M., and Peters, R. (1986) Molecular mobility and nucleocytoplasmic flux in hepatoma cells. *J. Cell Biol. 102*, 1183–90.

(27) Eliyahu, H., Joseph, A., Schillemans, J. P., Azzam, T., Domb, A. J., and Barenholz, Y. (2007) Characterization and in vivo performance of dextran-spermine polyplexes and DOTAP/cholesterol lipoplexes administered locally and systemically. *Biomaterials 28*, 2339–49.

(28) Fumoto, S., Kawakami, S., Shigeta, K., Higuchi, Y., Yamashita, F., and Hashida, M. (2005) Interaction with blood components plays a crucial role in asialoglycoprotein receptor-mediated in vivo gene transfer by galactosylated lipoplex. *J. Pharmacol. Exp. Ther. 315*, 484–93.

(29) Wu, J., Nantz, M. H., and Zern, M. A. (2002) Targeting hepatocytes for drug and gene delivery: emerging novel approaches and applications. *Front. Biosci. 7*, d717–25.

(30) Kim, H. R., Kim, I. K., Bae, K. H., Lee, S. H., Lee, Y., and Park, T. G. (2008) Cationic solid lipid nanoparticles reconstituted from low density lipoprotein components for delivery of siRNA. *Mol. Pharm. 5*, 622–31.

BC900150V

2918 *Biochemistry* **2010,** *49,* 2918–2924
DOI: 10.1021/bi902127u

BIOCHEMISTRY
including biophysical chemistry & molecular biology
Article

Effects of Introducing Fibrinogen Aα Character into the Factor XIII Activation Peptide Segment[†]

Madhavi A. Jadhav, Giulia Isetti, Toni A. Trumbo, and Muriel C. Maurer*

Department of Chemistry, University of Louisville, 2320 South Brook Street, Louisville, Kentucky 40292

Received December 11, 2009; Revised Manuscript Received February 22, 2010

ABSTRACT: The formation of a blood clot involves the interplay of thrombin, fibrinogen, and Factor XIII. Thrombin cleaves fibrinopeptides A and B from the N-termini of the fibrinogen Aα and Bβ chains. Fibrin monomers are generated that then polymerize into a noncovalently associated network. By hydrolyzing the Factor XIII activation peptide segment at the R37−G38 peptide bond, thrombin assists in activating the transglutaminase FXIIIa that incorporates cross-links into the fibrin clot. In this work, the kinetic effects of introducing fibrinogen Aα character into the FXIII AP segment were examined. Approximately 25% of fibrinogen Aα is phosphorylated at Ser3, producing a segment with improved binding to thrombin. FXIII AP (^{22}AEDDL^{26}) has sequence properties in common with Fbg Aα (^{1}ADSpGE^{5}). Kinetic benefits to FXIII AP cleavage were explored by extending FXIII AP (28−41) to FXIII AP (22−41) and examining peptides with D24, D24S, D24Sp, and D24Sp P27G. These modifications did not provide the same kinetic advantages that were observed with Fbg Aα (1−20) S3p. Such results further emphasize that FXIII AP derives most of its substrate specificity from the P_9−P_1 segment. To enhance the kinetic properties of FXIII AP (28−41), we introduced substitutions at the P_9, P_4, and P_3 positions. Studies reveal that FXIII AP (28−41) V29F, V34G, V35G exhibits kinetic improvements that are comparable to those of FXIII AP V29F, V34L and approach those of Fbg Aα (7−20). Selective changes to the FXIII AP segment sequence may be used to design FXIII species that can be activated more or less readily.

Thrombin, fibrinogen, and Factor XIII (FXIII)[1] play critical roles in the last stages of the blood coagulation cascade (*1*−*4*). Fibrinogen is a structural protein that circulates in the blood as a dimer of trimers [(AαBβγ)$_2$]. The serine protease thrombin cleaves the R16−G17 peptide bond of the fibrinogen Aα chains and the R14−G15 peptide bond of the fibrinogen Bβ chains, thereby releasing fibrinopeptides A and B. These cleavages lead to exposure of fibrin polymerization sites that promote formation of a noncovalently associated fibrin clot network. Thrombin also supports Factor XIII activation by hydrolyzing the FXIII R37−G38 peptide bond which later aids in exposure of the transglutaminase catalytic site (*3*, *4*). Activated FXIII catalyzes the formation of γ-glutamyl−ε-lysyl covalent cross-links in the fibrin network and in fibrin−enzyme complexes.

Thrombin is a versatile serine protease that targets several players in coagulation, anticoagulation, and platelet activation (*1*, *5*, *6*). This sodium-activated type II enzyme utilizes insertion loops on its surface to limit substrate access to the active site cleft. Moreover, thrombin contains two anion binding exosites (ABE-I and ABE-II) that it employs to promote interactions with selected proteins (Figure 1). For example, regions of fibrinogen Aα, PAR1, hirudin, and thrombomodulin bind to ABE-I, whereas fibrinogen γ′, heparin, GpIbα, and FVIII target ABE-II.

A review of thrombin substrates reveals that amino acids located N-terminal to the scissile bond make important contributions to binding and to rates of hydrolysis (*7*). The P_2, P_4, and P_9 positions[2] have been extensively studied. A common polymorphism exists in FXIII where a Val at the P_4 position is replaced with a Leu (V34L) (*3*). FXIII V34L is found in approximately 25% of the Caucasian population and results in a FXIII that is more easily activated by thrombin. This polymorphism has been correlated with protection against myocardial infarction (*3*, *4*). These effects occur predominantly under high-fibrin(ogen) conditions and are associated with thinner fibrin chains and a more permeable clot structure (*8*).

Our laboratory has utilized kinetic studies and solution NMR methods to probe the roles of individual FXIII AP residues in interacting with thrombin. Trends observed with synthetic peptide models of the FXIII V34 and FXIII V34L activation segment are in agreement with results obtained with their intact FXIII species (*9*−*13*). A series of peptides with substitutions at the P_4 position (V, L, F, A, and I) have been screened for reactivity (*14*, *15*). The cardioprotective L34 continues to provide the strongest k_{cat}/K_m due to enhancements in K_m and even stronger influences on k_{cat}. Two-dimensional (2D) trNOESY studies have

[†]Funding for this project was provided by National Institutes of Health Grant R01 HL68440.

*To whom correspondence should be addressed. Telephone: (502) 852-7008. Fax: (502) 852-8149. E-mail: muriel.maurer@louisville.edu.

[1]Abbreviations: FXIII, blood clotting Factor XIII; AP, activation peptide; Fbg Aα, fibrinogen Aα chain; PAR1, protease-activated receptor 1; PAR4, protease-activated receptor 4; RP-HPLC, reversed phase high-performance liquid chromatography; MALDI-TOF, matrix-assisted laser desorption ionization time-of-flight; K_m, Michaelis−Menten kinetic constant; k_{cat}, catalytic constant or turnover number; NMR, nuclear magnetic resonance; NOESY, nuclear Overhauser effect spectroscopy; PDB, Protein Data Bank; trNOESY, transferred NOESY.

[2]The P nomenclature system (...P_3, P_2, P_1, P_1', P_2', P_3', ...) is used to assign the individual amino acid positions on the substrate peptides. The P_1−P_1' peptide bond becomes hydrolyzed by the enzyme. The peptide amino acids N-terminal to the cleavage site are labeled P_2, P_3, P_4, etc., whereas those that are C-terminal are labeled P_2', P_3', P_4', etc.

 Published on Web 03/10/2010

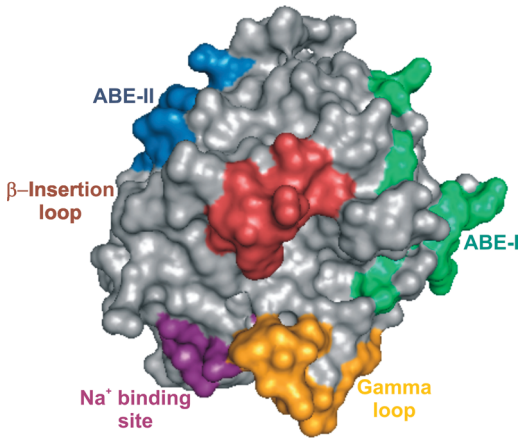

FIGURE 1: Structure of thrombin showing key surface loops and exosites. A contour representation of thrombin (PDB entry 1PPB) is displayed with the active site region in the center. β and γ loops that regulate substrate specificity and access to the catalytic site are colored maroon and yellow, respectively. Anion binding exosite I is located to the right of the active site region and is colored green, whereas anion binding exosite II is located to the left and is colored blue. The allosteric sodium binding site is colored purple. The molecular graphics program PyMOL was used to create the structures displayed in Figures 1−3.

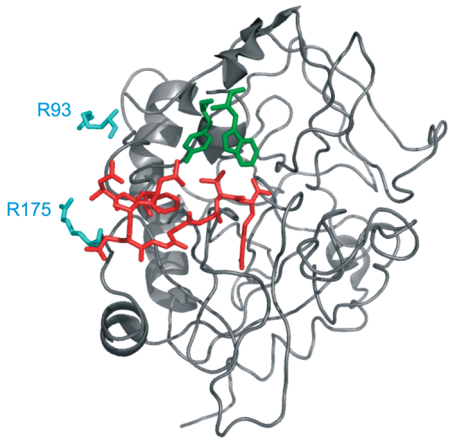

FIGURE 2: Evaluating thrombin interaction sites for the N-terminal Fbg Aα sequence. The X-ray crystal structure of human Fbg Aα (7−16) (red) bound to bovine thrombin (gray) is displayed (PDB entry 1BBR). The thrombin β-insertion loop residues Trp60d and Tyr60a are colored green. Two residues of anion binding exosite II (R93 and R175) that could accommodate Fbg Aα S3p are colored light blue.

revealed an important P_4−P_2 interaction (L34/F34−P36) that is proposed to promote interactions with the thrombin active site region (*11*, *15*).

In addition to the active site region, the anion binding exosites are also valuable to consider. A fibrinogen Aα region located C-terminal to the thrombin-cleaved scissile bond targets ABE-I (*2*, *5*). By contrast, phosphorylation near the N-terminus allows this fibrinogen chain to be accommodated by thrombin ABE-II (*16*). The fibrinogen Aα chain can be phosphorylated at two sites: the N-terminal S3 (*17*) and the more distant S345 (*18*). Increased levels of phosphorylation have been observed under certain physiological and pathophysiological conditions (*19*, *20*). Human fetal fibrinogen contains twice the degree of Aα phosphorylation of adult fibrinogen (*21*). The amount of phosphorylated fibrinogen has been reported to double following hip replacement surgery (*18*). Elevated levels of phosphorylated fibrinogen have also been observed in cancer patients and in individuals recovering from acute myocardial infarction (*22*−*25*).

Approximately 25−30% of plasma-derived human fibrinogen Aα (Fbg Aα) is phosphorylated at the Ser3 position (*26*, *27*). Similar levels have been found in human fibrinogen chains expressed in CHO cells, suggesting that partial phosphorylation is a native phenomenon (*28*). Kinetic studies of intact Fbg Aα and on Fbg Aα-like peptides [Aα (1−20)] have revealed that phosphorylation at the S3 position lowers the K_m of thrombin hydrolysis (*16*, *29*). Moreover, one-dimensional (1D) and 2D NMR studies have shown that Ser3p helps to anchor Aα (1−5) to the thrombin surface (*16*, *30*). A review of the Fbg Aα residues ^{1}ADS$_p$GE^{5} reveals that they have properties in common with FXIII AP (^{22}AEDDL^{26}). They both start with an alanine and then contain a series of negatively charged residues that could be accommodated by positively charged residues on an enzyme. These characteristics lead to an interest in exploring whether binding interactions between FXIII AP and the thrombin surface could be further enhanced via introduction of a site of phosphorylation in which D24 is replaced with a phosphorylated serine (D24Sp). It is already known that residues within the FXIII P_9−P_1 segment make important contributions to binding and hydrolysis. The possibility of obtaining additional benefits from targeting ABE-II warrants further investigation.

Another strategy for enhancing the binding and hydrolysis of FXIII AP would be to introduce more Fbg Aα-like character into the P_9−P_1 region. The Phe8 residue at the P_9 position of Fbg Aα is vital for generating its effective thrombin substrate properties (*31*, *32*). A characteristic helical turn structure (*33*) is adopted in which F8 is directed toward the P_4−P_1 region (^{13}GGVR^{16}) (Figure 2). V29F can be introduced into the FXIII AP sequence, but there is concern with regard to how well the aromatic residue can be accommodated by the ^{34}VVPR^{37} FXIII stretch (*11*). To alleviate possible steric issues, a FXIII AP peptide was proposed containing V29F, V34G, and V35G mutations. The Pro at the P_2 position would remain since this residue plays a key anchoring role in the FXIII activation peptide sequence. The new sequence would thus contain substitutions at the P_9, P_4, and P_3 positions.

This work supports the proposal that FXIII derives most of its substrate specificity from P_9−P_1 with a focus on the P_4−P_1 segment. FXIII activation peptides that are extended to the P_{16} position and further designed to target ABE-II do not exhibit the kinetic benefits observed for comparable fibrinogen Aα-like sequences. Introducing other characteristic features of the Aα chain into the FXIII AP segment is a more promising strategy for altering the activation properties of Factor XIII. For the mutant sequence FXIII AP (28−41) V29F, replacements of V34 and V35 with glycines promoted more effective binding and hydrolysis within the thrombin active site. Interestingly, the kinetic properties are comparable to those of FXIII AP (28−41) V29F, V34L. From these different studies, valuable information about the substrate specificity of thrombin for FXIII AP is being revealed.

EXPERIMENTAL PROCEDURES

Synthetic Peptides. Peptides based on residues 22−41 of the human FXIII activation peptide were synthesized by New England Peptide (Gardner, MA) or by Giulia Isetti (University of Louisville). The peptide based on residues 28−41 was synthesized by SynPep (Dublin, CA). The peptide sequences are as follows: FXIII AP (22−41), Ac-AEDDLPTVELQGVVPRGVNL-amide; FXIII AP (22−41) D24S, Ac-AESDLPTVELQGVVP-RGVNL-amide; FXIII AP (22−41) D24Sp, Ac-AESpDLPT-

VELQGVVPRGVNL-amide; FXIII AP (22−41) D24Sp P27G, Ac-AESpDLGTVELQGVVPRGVNL-amide; FXIII AP (28−41) V29F, V34G, V35G, Ac-TFELQGGGPRGVNL-amide. The purity of the peptides was evaluated by analytical reversed phase HPLC. MALDI-TOF mass spectrometry measurements on an Applied Biosystems Voyager DE-Pro mass spectrometer were used to verify the peptide m/z values. The concentrations of the peptide stock solutions were determined by quantitative amino acid analysis (AAA Service Laboratory, Damascus, OR, and University of Iowa, Molecular Analysis Facility, Iowa City, IA). All peptides were soluble to 8 mM.

Thrombin Preparation. Plasma bovine citrate or sulfate eluate (Sigma) was dissolved in 50 mM Tris, 150 mM NaCl, and 0.1% PEG (pH 7.4) and desalted on a GE Healthcare Biotech PD-10 column into the same buffer. The prothrombin-containing solution was then activated at 37 °C by *Echis carinatus* snake venom in the presence of $CaCl_2$. The ability to clot fibrinogen was monitored over time. A Sephadex G-25 column equilibrated with 25 mM H_3PO_4 and 100 mM NaCl (pH 6.5) was employed to desalt the venom-activated mixture. The generated thrombin was then purified on an Amersham Pharmacia Biotech Mono S cation exchange column (HR10/10) using a linear gradient from 0 to 1 M NaCl in 25 mM H_3PO_4 (pH 6.5). The pooled thrombin solution was concentrated by ultrafiltration, aliquoted, and stored at −70 °C. The final concentration of thrombin was determined using an extinction coefficient $E^{1\%}$ of 19.5 at 280 nm.

The bovine form of thrombin was used for this project, and the synthetic substrates were based on human sequences. There is a high degree of sequence conservation between bovine and human thrombin (*34*). No differences appear in the residues involving the active site, the thrombin β-insertion loop (also called the Trp^{60D} loop), or the allosteric Na^+ binding site. Any changes within ABE-II involve complementary substitutions between Lys and Arg residues. The other minor differences that do exist between the species are not anticipated to interfere with the interaction of the substrate peptides at the thrombin active site surface. Further supporting this notion, NMR studies (*35*−*37*) involving bovine thrombin and peptides targeting the active site (fibrinopeptide A and PAR1) have been in agreement with X-ray studies of the same peptides in the presence of human thrombin (*38*, *39*). Furthermore, NMR studies involving γ' peptides that target ABE-II have revealed similar results for both bovine α-IIa and human γ-IIa (*40*).

Kinetics Procedure. The HPLC-based kinetic assay methods described by Trumbo and Maurer (*9*) were employed. Briefly, a solution of peptide and assay buffer [50 mM H_3PO_4, 100 mM NaCl, and 0.1% PEG (pH 7.4)] was heated to 25 °C in a heat block. The peptide concentrations were within the range of 50−1500 μM for the FXIII AP (22−41) peptide series [D24, D24S, D24Sp, and D24Sp P27G]. For FXIII AP (28−41) V29F, V34G, V35G, the concentrations included 45−455 μM. Hydrolysis was started by the addition of bovine thrombin. The thrombin concentration for the hydrolysis reactions was 33.6 nM for the FXIII AP (22−41) peptide series and 2.2 nM for FXIII AP (28−41) V29F, V34G, V35G. At regular intervals, an aliquot of the reaction mixture was removed and quenched in 12.5% H_3PO_4. A Brownlee Aquapore Octyl RP-300 C_8 Cartridge column was used to separate the peptide peaks on a Waters HPLC system. The thrombin concentration and kinetic time points were chosen so that less than 15% of the total peptide concentration was hydrolyzed within 30 min. The FXIII AP (28−37) product peak was integrated and the peak area converted to concentration using a calibration curve.

The slopes of product concentration versus time plots were used to determine the initial velocities (in micromolar per second) for the different thrombin-catalyzed reactions. The results reported represent averages for at least three independent experiments. Kinetic values were calculated using nonlinear regression analysis fit to the equation $V = V_{max}/(1 + K_m/[S])$ using the Marquardt−Levenberg algorithm in Sigma Plot (Jandel Scientific). K_m, V_{max}, and k_{cat} were calculated from the coefficients of this equation. ANOVA calculations followed by Tukey−Kramer multiple comparisons were utilized for statistical analysis of the kinetics data (GraphPad, InStat Biostatistics, version 3.0). The different kinetic constants determined for the current project were examined relative to values obtained from previous published studies that had all been conducted with bovine thrombin.

RESULTS

Thrombin-Catalyzed Hydrolysis of FXIII Activation Peptides. An HPLC assay was used to monitor the hydrolysis rates of peptides based on FXIII AP (22−41) and peptide FXIII AP (28−41) V29F, V34G, V35G. For each peptide, thrombin cleaved at the R37−G38 amide bond and the substrates and hydrolyzed products eluted as distinct peaks on the Brownlee Aquapore C_8 column. Hydrolyzed segments corresponding to FXIII AP (22−37) and FXIII AP (28−37) were verified by MALDI-TOF mass spectrometry. Accumulation of these individual products over time was used in the kinetic fit calculations.

Kinetic Analysis of FXIII AP Peptides That Could Extend from the Thrombin Active Site toward Anion Binding Exosite II. Earlier studies in our laboratory reported the kinetic parameters associated with thrombin hydrolysis of FXIII AP (28−41) (*9*). In the study presented here, the FXIII AP segment length was increased N-terminally to FXIII AP (22−41). Table 1 displays this sequence along with others related to this project. Nonlinear regression analysis values for K_m, k_{cat}, and k_{cat}/K_m are listed in Table 2. The seven additional N-terminal residues present in FXIII AP (22−41) contributed to a 1.7-fold decrease in K_m relative to FXIII AP (28−41) ($P < 0.001$). This decrease corresponded to a moderate improvement in binding interactions.

A phosphorylated S3 at the P_{14} position of Fbg Aα (1−20) is known to promote binding of this peptide substrate to thrombin (*16*, *29*). FXIII AP (22−41) contains a D24 at the same position as S3 of Fbg Aα (1−20). A FXIII AP (22−41) D24S substitution was well-tolerated, and the kinetic binding properties remained statistically different from those of FXIII AP (28−41) ($P < 0.01$). Introducing a site of phosphorylation at S24 (D24Sp) resulted in some minor increases in K_m. Upon reviewing the FXIII AP (22−41) D24Sp sequence, we were concerned that the P27 residue might promote a turn structure that hinders optimal interactions with thrombin ABE-II. To alleviate this possibility and introduce more flexibility, a glycine was introduced to produce FXIII AP (22−41) D24Sp P27G. Only a very minor improvement in K_m occurred relative to FXIII AP (22−41) D24Sp. A review of the kinetic data revealed that there were no statistical differences in K_m values among the different variants of FXIII AP (22−41).

The k_{cat} values also provided valuable information about interactions between the FXIII AP segments and thrombin. The N-terminal extension to FXIII AP (28−41) to generate FXIII AP (22−41) resulted in a minor 1.3-fold decrease in k_{cat}

Table 1: Substrate Sequences Capable of Extending to Thrombin ABE-II[a]

	P_9.....P_4.....P_1...
Factor XIII AP (22-41)	^{22}AED DLPTVELQGVVPRGVNL^{41}
Factor XIII AP (22-41) D24S	^{22}AES DLPTVELQGVVPRGVNL^{41}
Factor XIII AP (22-41) D24S$_p$	^{22}AES$_p$DLPTVELQGVVPRGVNL^{41}
Factor XIII AP (22-41) D24S$_p$ P27G	^{22}AES$_p$DLGTVELQGVVPRGVNL^{41}
Fibrinogen Aα (1-20) S3$_p$	^{1}ADS$_p$GEGDFLAEGGGVRGPRV^{20}

[a]Human sequences of factor XIII and fibrinogen Aα are displayed. Sp corresponds to a phosphorylated serine.

Table 2: Kinetic Constants for Hydrolysis of FXIII AP Substrates Capable of Extending to Thrombin ABE-II[a]

peptide sequence	K_m (μM)	k_{cat} (s^{-1})	k_{cat}/K_m (s^{-1} μM^{-1})
FXIII AP (28−41)[b]	508 ± 44	6.4 ± 0.03	0.013 ± 0.001
FXIII AP (22−41)	300 ± 54	4.9 ± 0.01	0.016 ± 0.003
FXIII AP (22−41) D24S	270 ± 43	4.7 ± 0.31	0.017 ± 0.003
FXIII AP (22−41) D24Sp	422 ± 65	6.9 ± 0.48	0.016 ± 0.003
FXIII AP (22−41) D24Sp P27G	370 ± 34	3.5 ± 0.15	0.009 ± 0.001

[a]Kinetic constants for the thrombin-catalyzed hydrolysis reactions were determined from an HPLC assay as described in Experimental Procedures. The results shown here represent averages of at least three independent experiments. Kinetic values were calculated using nonlinear regression analysis methods using SigmaPlot. The error values correspond to the standard error of the mean (SEM). [b]From ref *9*.

($P > 0.05$). This value was maintained with the D24S substitution. The k_{cat} value for FXIII AP (22−41) D24Sp increased to that of FXIII AP (28−41). The additional P27G mutation generated a FXIII AP (22−41) D24Sp P27G peptide that exhibited an ~2-fold decrease in the k_{cat} value relative to that of FXIII AP (28−41). A convincing case for statistical differences in the k_{cat} values of the FXIII AP (28−41) and (22−41) peptide series could not be found.

Introducing Fibrinogen Aα-like Character into FXIII AP (28−41). Prior studies evaluated the effects of introducing V29F into FXIII AP (28−41), thus placing an aromatic residue (*11*) at the same position as the vital F8 of Fbg Aα (7−20) (Tables 3 and 4). The K_m value for hydrolysis of FXIII AP (28−41) V29F improved 2.6-fold relative to that of wild-type FXIII AP (28−41) ($P < 0.01$), whereas the k_{cat} value remained virtually unchanged. In the study presented here, additional features of the Fbg Aα chain were introduced. The newly modified FXIII AP segment contained the Phe residue (V29F), and the aliphatic branched V34 and V35 residues were replaced with smaller G34 and G35 residues, respectively [FXIII AP V29F, V34G, V35G (T*F*ELQG*GG*PRGVNL, mutated residues in italics)]. The K_m of FXIII AP V29F, V34G, V35G (326 ± 79 μM) was between that of FXIII AP (28−41) (508 ± 44 μM) and that of FXIII AP (28−41) V29F (195 ± 34 μM) ($P < 0.01$ for both comparisons). By contrast, the k_{cat} value of FXIII AP (22−41) V29F, V34G, V35G increased 4.5-fold relative to those of FXIII AP (28−41) and FXIII AP (28−41) V29F ($P < 0.001$). An evaluation of the resultant k_{cat}/K_m values revealed that the substrate specificity toward FXIII AP (28−41) V29F, V34G, V35G was significantly different ($P < 0.001$) from that of FXIII activation peptides containing a V34G, V29F, or V34L substitution (Table 4). Interestingly, the K_m value of FXIII AP (28−41) V29F, V34G, V35G was now comparable to that of Fbg Aα (7−20). Furthermore, the k_{cat} had improved such that it was now only 1.4-fold lower than that of Fbg Aα (7−20).

Table 3: Introducing Fibrinogen Aα-like Character into the Factor XIII Activation Peptide[a]

	P_9.....P_4....P_1...
Factor XIII AP (28-41)	^{28}TVELQGVVPRGVNL^{41}
Factor XIII AP (28-41) V34L	^{28}TVELQGLVPRGVNL^{41}
Factor XIII AP (28-41) V29F	^{28}TFELQGVVPRGVNL^{41}
Factor XIII AP (28-41) V29F V34L	^{28}TFELQGLVPRGVNL^{41}
Factor XIII AP (28-41) V29F, V34G, V35G	^{28}TFELQGGGPRGVNL^{41}
Fibrinogen Aα (7-20)	^{7}DFLAEGGGVRGPRV^{20}

[a]Human sequences for factor XIII and fibrinogen Aα are displayed.

Table 4: Kinetic Constants for Hydrolysis of FXIII AP Substrates Having Fibrinogen Aα-like Character[a]

peptide sequence	K_m (μM)	k_{cat} (s^{-1})	k_{cat}/K_m (s^{-1} μM^{-1})
FXIII AP (28−41)[b]	508 ± 44	6.4 ± 0.03	0.013 ± 0.001
FXIII AP (28−41) V34L[b]	272 ± 57	18.5 ± 1.6	0.068 ± 0.02
FXIII AP (28−41) V29F[c]	195 ± 34	6.2 ± 0.4	0.032 ± 0.006
FXIII AP (28−41) V29F, V34L[c]	352 ± 77	27.5 ± 2.9	0.078 ± 0.02
FXIII AP (28−41) V29F, V34G, V35G	326 ± 79	28.6 ± 3.7	0.088 ± 0.02
Fbg Aα (7−20)[b]	312 ± 42	39.3 ± 2.6	0.126 ± 0.02

[a]Kinetic constants for the thrombin-catalyzed hydrolysis reactions were determined from an HPLC assay as described in Experimental Procedures. The results shown here represent averages of at least three independent experiments. Kinetic values were calculated using nonlinear regression analysis methods using SigmaPlot. The error values correspond to the standard error of the mean (SEM). [b]From ref *9*. [c]From ref *11*.

DISCUSSION

Factor XIII is activated in part when the serine protease thrombin cleaves the FXIII R37−G38 peptide bond (*2*−*4*). This work provides an opportunity to evaluate the extent to which additional features from Fbg Aα, a major physiological substrate, can be introduced into the FXIII AP sequence to promote binding interactions (K_m) and/or catalytic turnover (k_{cat}). The knowledge gained may be used in the design of new FXIII AP segments that can be activated to different extents.

Evaluating Whether FXIII AP Segments That Take Advantage of Binding to Anion Binding Exosite II Can Be Generated. A review of the FXIII AP sequence reveals that the N-terminal segment (^{22}AEDDL^{26}) has negative charge character resembling that of the N-terminal Fbg Aα segment (^{1}ADSGE^{5}). The N-terminal Fbg Aα (1−5) segment is quite flexible and designed to permit multiple conformations depending on the environment encountered. NMR and docking studies suggest that introducing a phosphoserine at position 3 (S3p) encourages contact with the thrombin surface. The phosphate is proposed to bind in the vicinity of R175 and R93 (*16*) (Figures 1 and 2). In response to the new substrate anchor point, a valuable improvement in the K_m value occurs (*16*).

For this study, the features of Fbg Aα S3p were systematically introduced into the FXIII AP D24 position. Prior work had focused on FXIII AP (28−37) and on the truncated FXIII AP

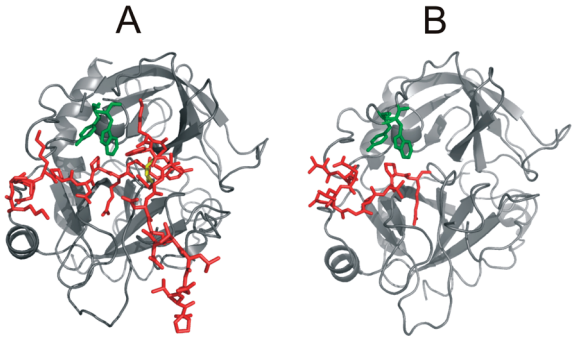

FIGURE 3: Comparison of the conformational features of two thrombin−substrate complexes. (A) Cartoon representation of murine PAR4 (51−81) (red) bound to murine thrombin (gray) (PDB entry 2PV9). Pro62 which is hypothesized to play a role in redirecting the PAR4 segment from the active site toward the thrombin autolysis loop is colored yellow. Thrombin β-insertion loop residues Trp60d and Tyr60a are colored green. (B) Cartoon representation of the X-ray crystal structure of FXIII AP (28−37) (red) bound to thrombin (gray) (PDB entry 1DE7). Thrombin β-insertion loop residues Trp60d and Tyr60a are colored green. So far, the helical-turn conformation captured in the crystal structure has not been observed in solution by NMR methods.

(33−37) sequence (*9*, *41*). Extending the FXIII AP segment toward A22 at the P_{16} position did provide some benefits to K_m, but the k_{cat} was negatively affected. A D24S substitution was well-tolerated, indicating that an acidic aspartate residue was not required for the P_{14} position of FXIII AP. Introducing the phosphorylated Ser (D24Sp) generated modest improvements in k_{cat}, but the K_m also increased. Overall, the slight improvements in k_{cat}/K_m obtained with the N-terminal extension and the site of phosphorylation were not statistically significant (Table 2).

A recent X-ray crystal structure of a murine PAR4 segment (^{51}K−A^{81}) bound to murine thrombin (Figure 3A) revealed an important conformational feature to consider (*42*). G60 located at the P_1' position of this substrate sequence helps to initiate a turn followed by a short helical segment. Instead of extending from the thrombin active site to ABE-I, the PAR4 segment is redirected toward the thrombin autolysis loop located below the entrance to the active site. P62 plays a critical role in helping to achieve this structural change (see the residue colored yellow in Figure 3A). Interestingly, the FXIII AP segment contains a stretch with a Pro residue at the P_{11} position (^{22}AEDDLPTVEL^{31}). This ring structure may hinder the ability of the phosphorylated FXIII AP segment to target a complementary Arg or Lys residue within thrombin ABE-II (*16*). Extra flexibility was introduced through the D24Sp P27G double mutant, but the new sequence did not provide extensive benefits. If anything, an ability to orient effectively within the thrombin active site region had become hindered.

The results obtained with this sequence design project lead to a reanalysis of the properties of FXIII and fibrinogen Aα. When bound to thrombin, the fibrinogen Aα segment (^{1}ADSGEGDFLAEGGGVR^{16}) adopts a unique helical-turn structure (*33*) with key participation from F8, L9, and ^{13}GGVR^{16} (Figure 2). Such a structure has not been observed in solution NMR studies of FXIII AP V34, V34L, or V34F bound to thrombin (*11*, *15*). Fbg Aα clearly requires an extension out to at least the P_9 residue and can gain further benefits by proceeding to the P_{16} position and utilizing S3p at the P_{14} position. By contrast, kinetic studies with FXIII AP (22−41), FXIII AP (28−41), and the truncated segment FXIII AP (33−41) indicate that thrombin takes advantage of the P_9−P_1 residues with a focus on the P_4−P_1 region (*41*). Furthermore, results suggest that FXIII residues surrounding the P_4 position are more important for controlling thrombin binding and hydrolysis than extending to a segment that could target ABE-II.

Evaluating the Effects of the Introduction of Further Fbg Aa-like Character into FXIII AP (*28*−*41*). The roles of the P_9−P_1 positions in promoting thrombin-catalyzed hydrolysis of FXIII AP segments are worth further exploring. The common V34L polymorphism results in a 2-fold improvement in K_m and more importantly a 3-fold improvement in k_{cat} relative to those of FXIII AP V34 (*9*) (Table 4). Overall, a 5-fold improvement in k_{cat}/K_m occurs with the addition of a methylene group to V34 at the P_4 position. Introduction of V29F at the P_9 position (*11*) leads to a 2.6-fold improvement in K_m relative to that of FXIII AP (28−41) V34; however, there is no change to k_{cat}. Although the V29F substitution makes the FXIII AP segment more Fbg Aα-like, the kinetic benefits found in the Aα chain have not been achieved. Moreover, the characteristic helical-turn structure of Fbg Aα (7−16) is not observed in solution NMR studies of FXIII AP (28−37) V29F bound to thrombin (*15*).

To help promote the optimal orientation of the FXIII V29F AP segment at the thrombin active site, the V34 and V35 residues at the P_4 and P_3 positions, respectively, were replaced with glycines. Some decreases in the level of binding interaction were observed, but more impressively, there was a 4.5-fold enhancement in catalytic turnover. To further improve k_{cat}, the next residue to mutate might be the P_2 position. Difficulties, however, will likely arise since FXIII AP (28−41) P36V exhibits solubility issues.

Unexpectedly, the kinetic properties of the FXIII AP (28−41) V29F, V34G, V35G peptide (^{28}TFELQGGGPRGVNL^{41}) are very similar to those of FXIII AP (28−41) V29F, V34L (^{28}TFELQGLVPRGVNL^{41}) (*11*). For each sequence, the P_9 and P_4−P_1 residues are underlined. Both peptides have comparable K_m values, and they both exhibit the 4.5-fold improvement in k_{cat} over that of FXIII AP (28−41) V34. In an earlier publication, the V34L substitution at the P_4 position was proposed to play a more critical role than the V29F substitution at the P_9 position (*11*). The V34L substitution could influence K_m and k_{cat}, whereas the V29F substitution could influence only K_m. Solution NMR studies indicated that the hallmark P_4−P_2 interaction involving L34 and P36 was preserved in FXIII AP V29F, V34L and a helical turn involving F29 was still not visible (*11*). These studies suggest that V34G and V35G substitutions at the P_4 and P_3 positions, respectively, can mimic the kinetic benefits of the V34L substitution at the P_4 position. The P_3 position exhibits much sequence variability and might not be expected to make a major contribution to substrate specificity. Work by Lee et al. (*43*) revealed that recombinant FXIII A_2 V35L (at P_3) does not exhibit the kinetic benefits of the V34L substitution. By contrast, Andersen and co-workers (*44*) reported that recombinant FXIII A_2 V34L, V35T results in a 7.6-fold increase in activation rate relative to that of FXIII A_2 V34 and a 5-fold increase relative to that of FXIII A_2 V34L. Our research indicates another P_4−P_3 double substitution (V34G, V35G) that can exhibit beneficial effects toward thrombin-catalyzed hydrolysis of the FXIII AP segment. The improvements with FXIII AP V29F, V34G, V35G are comparable to those with FXIII AP V29F, V34L.

Determining the structural features of thrombin-bound FXIII AP (28−37) V29F, V34G, V35G and comparing them to the previously published FXIII AP sequences would be valuable.

Unfortunately, it has not been possible to examine the triply substituted peptide using 1D proton line broadening and 2D trNOESY. The peptide does not exhibit sufficiently fast exchange on and off the enzyme surface. This slow exchange does, however, support the proposal that the substitutions at the P_9, P_4, and P_3 positions have generated a peptide that exhibits increased affinity for the thrombin surface.

The ability to create a FXIII AP (28−41) segment that mimics the properties of Fbg Aα (7−20) leads to the question of whether a true hybrid FXIII AP−Fbg Aα sequence could be effective. Andersen and co-workers recently published their results on such a system (*44*). Fbg Aα (7−15) and Aα (7−20) were incorporated into recombinant FXIII A_2 in place of the FXIII AP (28−37) or FXIII AP (28−41) segment. Interestingly, these variants had thrombin activation rates that were 5% of that of wild-type FXIII A_2. Furthermore, they exhibited greatly reduced clot lysis times.

To be an effective thrombin substrate, the Fbg Aα (7−20) segment must be able to adopt a turn conformation bringing F8 into the proximity of the R16−G17 cleavage site. This structural feature has been documented by both X-ray (*33*) and solution NMR methods (*35*, *36*). So far, a helical-turn conformation has not been observed in solution (*11*, *15*) with FXIII AP (28−37) V34, V34L, V34F, V29F, or the doubly substituted V29F, V34L form. If such a conformation does exist, it must be fleeting in nature. An X-ray crystal structure of a thrombin−FXIII AP (28−37) V34 complex has captured this structural feature (*45*) (Figure 3B). This backbone conformation occurs even though the degree of sequence identity of the P_{10}−P_1 residues of Fbg Aα (7−16) and FXIII AP (28−37) is only 20% (*46*). By contrast, FXIII AP (28−37) V34L appears to adopt a more extended conformation within the crystal complex (*45*). Molecular docking studies (*46*) have further supported this type of structural feature for a V34L substitution-containing activation peptide.

The FXIII AP segment is 37 residues in length, and X-ray crystallography of the intact protein suggests that each activation peptide straddles the FXIII dimer interface (*47*). With the hybrid FXIII AP−Fbg Aα sequence, it is highly likely that a helical turn must form for this segment to become an effective thrombin substrate. The low observed FXIII A_2 activation rates suggest there may be difficulties in achieving this conformational feature. The length of the FXIII AP segment may also be considered. The Fbg Aα segment contains only six residues N-terminal to the Fbg Aα (7−20) segment. The Fbg Aα (1−5) stretch is proposed to be highly flexible but can be anchored to thrombin ABE-II through phosphorylation at S3p (*16*). The FXIII AP (1−27) segment is so much longer. It is not known how well a helical turn could be maintained with residues 28−37 and the extent to which the conformation and placement of residues 1−27 would be affected.

Results with the hybrid FXIII AP−Fbg Aα demonstrate that the complete P_9−P_1 segment of Fbg Aα cannot be introduced successfully into intact FXIII A_2 (*44*). A strategy in which only a few residues are changed may be more effective in generating a FXIII with improved activation rates. In this work, an effort has been made to keep P36 as a P_2 anchor point and then to make selective changes to the P_9, P_4, or P_4/P_3 position. The peptides generated do not appear to have a requirement for a helical-turn structure, yet they can achieve kinetic parameters that approach those of Fbg Aα (7−20). These sequences have the potential for being more successful candidates within FXIII A_2.

Conclusions. Kinetic studies of the roles of individual substrate positions are highly worthwhile for understanding the sources of thrombin specificity. Introducing a site of phosphorylation at the P_{14} position of the thrombin substrate FXIII AP does not provide the benefits that are seen with a complementary Fbg Aα sequence. Extra anchoring of FXIII toward the ABE-II region may not be needed. Moreover, additional competing interactions with thrombin ABE-II may not be physiologically attractive. For promoting initial fibrin formation, it may be more desirable to use the exosite to enhance fibrinopeptide A cleavage.

This study also further supports the proposal that FXIII AP derives most of its substrate specificity from P_9−P_1 with a strong focus on the P_4−P_1 segment. The influential role of the P_4 position is well-documented. The FXIII AP segment can be further optimized via addition of other Fbg Aα-like features. A V29F substitution introduces an aromatic residue that can promote binding interactions with the extended thrombin active site surface. Additional improvements can come with FXIII AP V29F, V34G, V35G. The fact that a V29F and V34L substitution can also mimic such effects reinforces the critical role that the common L34 polymorphism plays in promoting the kinetic properties of the FXIII AP segment. So far, the vital helical-turn conformation of Fbg Aα (7−16) has not been observed in solution for FXIII AP segments bound to thrombin. Selective changes to the FXIII AP sequence that are not reliant on this distinct structural feature may provide greater versatility in the design of new FXIII species. This research has focused on amino acid substitutions to enhance K_m and/or k_{cat}, whereas other residue changes would be needed to generate a FXIII that is more difficult to activate. The final architecture of a fibrin clot will be influenced by thrombin's interplay with components of fibrinogen $(A\alpha B\beta\gamma)_2$ and the FXIII AP segment.

ACKNOWLEDGMENT

We appreciate helpful research discussions and critical evaluation of the manuscript from T. M. Sabo, R. Woofter, and P. Doiphode. We also thank R. Woofter for assistance in the statistical analysis of the data.

REFERENCES

1. Di Cera, E. (2007) Thrombin as procoagulant and anticoagulant. *J. Thromb. Haemostasis 5* (Suppl. 1), 196–202.
2. Weisel, J. W. (2005) Fibrinogen and fibrin. *Adv. Protein Chem. 70*, 247–299.
3. Ariens, R. A., Lai, T. S., Weisel, J. W., Greenberg, C. S., and Grant, P. J. (2002) Role of factor XIII in fibrin clot formation and effects of genetic polymorphisms. *Blood 100*, 743–754.
4. Muszbek, L., Bagoly, Z., Bereczky, Z., and Katona, E. (2008) The involvement of blood coagulation factor XIII in fibrinolysis and thrombosis. *Cardiovasc. Hematol. Agents 6*, 190–205.
5. Lane, D. A., Philippou, H., and Huntington, J. A. (2005) Directing thrombin. *Blood 106*, 2605–2612.
6. Di Cera, E. (2008) Thrombin. *Mol. Aspects Med. 29*, 203–254.
7. Backes, B. J., Harris, J. L., Leonetti, F., Craik, C. S., and Ellman, J. A. (2000) Synthesis of positional-scanning libraries of fluorogenic peptide substrates to define the extended substrate specificity of plasmin and thrombin. *Nat. Biotechnol. 18*, 187–193.
8. Lim, B. C., Ariens, R. A., Carter, A. M., Weisel, J. W., and Grant, P. J. (2003) Genetic regulation of fibrin structure and function: complex gene-environment interactions may modulate vascular risk. *Lancet 361*, 1424–1431.
9. Trumbo, T. A., and Maurer, M. C. (2000) Examining thrombin hydrolysis of the factor XIII activation peptide segment leads to a proposal for explaining the cardioprotective effects observed with the factor XIII V34L mutation. *J. Biol. Chem. 275*, 20627–20631.
10. Ariens, R. A., Philippou, H., Nagaswami, C., Weisel, J. W., Lane, D. A., and Grant, P. J. (2000) The factor XIII V34L polymorphism accelerates thrombin activation of factor XIII and affects cross-linked fibrin structure. *Blood 96*, 988–995.
11. Trumbo, T. A., and Maurer, M. C. (2002) Thrombin hydrolysis of V29F and V34L mutants of factor XIII (28−41) reveals roles of the P(9)

and P(4) positions in factor XIII activation. *Biochemistry 41*, 2859–2868.
12. Balogh, I., Szoke, G., Karpati, L., Wartiovaara, U., Katona, E., Komaromi, I., Haramura, G., Pfliegler, G., Mikkola, H., and Muszbek, L. (2000) Val34Leu polymorphism of plasma factor XIII: Biochemistry and epidemiology in familial thrombophilia. *Blood 96*, 2479–2486.
13. Wartiovaara, U., Mikkola, H., Szoke, G., Haramura, G., Karpati, L., Balogh, I., Lassila, R., Muszbek, L., and Palotie, A. (2000) Effect of Val34Leu polymorphism on the activation of the coagulation factor XIII-A. *Thromb. Haemostasis 84*, 595–600.
14. Trumbo, T. A., and Maurer, M. C. (2003) V34I and V34A substitutions within the factor XIII activation peptide segment (28−41) affect interactions with the thrombin active site. *Thromb. Haemostasis 89*, 647–653.
15. Isetti, G., and Maurer, M. C. (2004) Probing thrombin's ability to accommodate a V34F substitution within the factor XIII activation peptide segment (28−41). *J. Pept. Res. 63*, 241–252.
16. Maurer, M. C., Peng, J. L., An, S. S., Trosset, J. Y., Henschen-Edman, A., and Scheraga, H. A. (1998) Structural examination of the influence of phosphorylation on the binding of fibrinopeptide A to bovine thrombin. *Biochemistry 37*, 5888–5902.
17. Blombaeck, B., Blombaeck, M., Edman, P., and Hessel, B. (1962) Amino-acid sequence and the occurrence of phosphorus in human fibrinopeptides. *Nature 193*, 833–834.
18. Seydewitz, H. H., Kaiser, C., Rothweiler, H., and Witt, I. (1984) The location of a second in vivo phosphorylation site in the A α-chain of human fibrinogen. *Thromb. Res. 33*, 487–498.
19. Martin, S. C., Ekman, P., Forsberg, P. O., and Ersmark, H. (1992) Increased phosphate content of fibrinogen in vivo correlates with alteration in fibrinogen behaviour. *Thromb. Res. 68*, 467–473.
20. Seydewitz, H. H., and Witt, I. (1985) Increased phosphorylation of human fibrinopeptide A under acute phase conditions. *Thromb. Res. 40*, 29–39.
21. Witt, I., and Muller, H. (1970) Phosphorus and hexose content of human foetal fibrinogen. *Biochim. Biophys. Acta 221*, 402–404.
22. Gordon, I. O., and Freedman, R. S. (2006) Defective antitumor function of monocyte-derived macrophages from epithelial ovarian cancer patients. *Clin. Cancer Res. 12*, 1515–1524.
23. Wang, X., Wang, E., Kavanagh, J. J., and Freedman, R. S. (2005) Ovarian cancer, the coagulation pathway, and inflammation. *J. Transl. Med. 3*, 25.
24. Haglund, A. C., Ronquist, G., Frithz, G., and Ek, P. (2000) Alteration of the fibrinogen molecule and its phosphorylation state in myocardial infarction patients undergoing thrombolytic treatment. *Thromb. Res. 98*, 147–156.
25. Ogata, Y., Heppelmann, C. J., Charlesworth, M. C., Madden, B. J., Miller, M. N., Kalli, K. R., Cilby, W. A., Robert Bergen, H., III., Saggese, D. A., and Muddiman, D. C. (2006) Elevated levels of phosphorylated fibrinogen α-isoforms and differential expression of other post-translationally modified proteins in the plasma of ovarian cancer patients. *J. Proteome Res. 5*, 3318–3325.
26. Blomback, B., Blomback, M., Edman, P., and Hessel, B. (1966) Human fibrinopeptides. Isolation, characterization and structure. *Biochim. Biophys. Acta 115*, 371–396.
27. Blomback, B., Blomback, M., and Searle, J. (1963) On the occurrence of phosphorus in fibrinogen. *Biochim. Biophys. Acta 74*, 148–151.
28. Binnie, C. G., Hettasch, J. M., Strickland, E., and Lord, S. T. (1993) Characterization of purified recombinant fibrinogen: Partial phosphorylation of fibrinopeptide A. *Biochemistry 32*, 107–113.
29. Hanna, L. S., Scheraga, H. A., Francis, C. W., and Marder, V. J. (1984) Comparison of structures of various human fibrinogens and a derivative thereof by a study of the kinetics of release of fibrinopeptides. *Biochemistry 23*, 4681–4687.
30. Ni, F., Konishi, Y., Frazier, R. B., Scheraga, H. A., and Lord, S. T. (1989) High-resolution NMR studies of fibrinogen-like peptides in solution: Interaction of thrombin with residues 1−23 of the A α-chain of human fibrinogen. *Biochemistry 28*, 3082–3094.
31. Scheraga, H. A. (1983) Interaction of thrombin and fibrinogen and the polymerization of fibrin monomer. *Ann. N.Y. Acad. Sci. 408*, 330–343.
32. Scheraga, H. A. (1986) Chemical basis of thrombin interactions with fibrinogen. *Ann. N.Y. Acad. Sci. 485*, 124–133.
33. Martin, P. D., Robertson, W., Turk, D., Huber, R., Bode, W., and Edwards, B. F. (1992) The structure of residues 7−16 of the A α-chain of human fibrinogen bound to bovine thrombin at 2.3-Å resolution. *J. Biol. Chem. 267*, 7911–7920.
34. Bode, W., Turk, D., and Karshikov, A. (1992) The refined 1.9-Å X-ray crystal structure of D-Phe-Pro-Arg chloromethylketone-inhibited human α-thrombin: Structure analysis, overall structure, electrostatic properties, detailed active-site geometry, and structure-function relationships. *Protein Sci. 1*, 426–471.
35. Ni, F., Meinwald, Y. C., Vasquez, M., and Scheraga, H. A. (1989) High-resolution NMR studies of fibrinogen-like peptides in solution: Structure of a thrombin-bound peptide corresponding to residues 7−16 of the A α-chain of human fibrinogen. *Biochemistry 28*, 3094–3105.
36. Ni, F., Zhu, Y., and Scheraga, H. A. (1995) Thrombin-bound structures of designed analogs of human fibrinopeptide A determined by quantitative transferred NOE spectroscopy: A new structural basis for thrombin specificity. *J. Mol. Biol. 252*, 656–671.
37. Ni, F., Ripoll, D. R., Martin, P. D., and Edwards, B. F. (1992) Solution structure of a platelet receptor peptide bound to bovine α-thrombin. *Biochemistry 31*, 11551–11557.
38. Mathews, I. I., Padmanabhan, K. P., Ganesh, V., Tulinsky, A., Ishii, M., Chen, J., Turck, C. W., Coughlin, S. R., and Fenton, J. W., II. (1994) Crystallographic structures of thrombin complexed with thrombin receptor peptides: Existence of expected and novel binding modes. *Biochemistry 33*, 3266–3279.
39. Stubbs, M. T., Oschkinat, H., Mayr, I., Huber, R., Angliker, H., Stone, S. R., and Bode, W. (1992) The interaction of thrombin with fibrinogen. A structural basis for its specificity. *Eur. J. Biochem. 206*, 187–195.
40. Sabo, T. M., Farrell, D. H., and Maurer, M. C. (2006) Conformational analysis of γ′ peptide (410−427) interactions with thrombin anion binding exosite II. *Biochemistry 45*, 7434–7445.
41. Isetti, G., and Maurer, M. C. (2004) Thrombin activity is unaltered by N-terminal truncation of factor XIII activation peptides. *Biochemistry 43*, 4150–4159.
42. Bah, A., Chen, Z., Bush-Pelc, L. A., Mathews, F. S., and Di Cera, E. (2007) Crystal structures of murine thrombin in complex with the extracellular fragments of murine protease-activated receptors PAR3 and PAR4. *Proc. Natl. Acad. Sci. U.S.A. 104*, 11603–11608.
43. Lee, I. H., Chung, S. I., and Lee, S. Y. (2002) Effects of Val34Leu and Val35Leu polymorphism on the enzyme activity of the coagulation factor XIII-A. *Exp. Mol. Med. 34*, 385–390.
44. Andersen, M. D., Kjalke, M., Bang, S., Lautrup-Larsen, I., Becker, P., Andersen, A. S., Olsen, O. H., and Stennicke, H. R. (2009) Coagulation factor XIII variants with altered thrombin activation rates. *Biol. Chem. 390*, 1279–1283.
45. Sadasivan, C., and Yee, V. C. (2000) Interaction of the factor XIII activation peptide with α-thrombin. Crystal structure of its enzyme-substrate analog complex. *J. Biol. Chem. 275*, 36942–36948.
46. Nair, D. G., Sunilkumar, P. N., and Sadasivan, C. (2008) Modeling of factor XIII activation peptide (28−41) V34L mutant bound to thrombin. *J. Biomol. Struct. Dyn. 26*, 387–394.
47. Yee, V. C., Pedersen, L. C., Bishop, P. D., Stenkamp, R. E., and Teller, D. C. (1995) Structural evidence that the activation peptide is not released upon thrombin cleavage of factor XIII. *Thromb. Res. 78*, 389–397.